From orogen to passive margin: constraints from fission track and (U–Th)/He analyses on Mesozoic uplift and fault reactivation in SW Norway

ANNA K. KSIENZYK[1]*, ISTVÁN DUNKL[2], JOACHIM JACOBS[1], HAAKON FOSSEN[1,3] & FABIAN KOHLMANN[1]

[1]*Department of Earth Science, University of Bergen, PO Box 7803, 5020 Bergen, Norway*

[2]*Geoscience Centre, University of Göttingen, Goldschmidtstraße 3, 37077 Göttingen, Germany*

[3]*Natural History Collections, University Museum of Bergen, University of Bergen, PO Box 7800, 5020 Bergen, Norway*

**Corresponding author (e-mail: anna.ksienzyk@geo.uib.no)*

Abstract: The post-Caledonian tectonic history and landscape evolution of southwestern Norway are poorly understood, primarily owing to the lack of onshore post-Devonian sediments. To bridge this knowledge gap, low-temperature thermochronological techniques were applied to investigate vertical movements in the upper crust. New apatite fission track and apatite and zircon (U–Th)/He analyses on samples from southwestern Norway yielded Permian to Jurassic, Triassic to Cretaceous and Carboniferous to Triassic ages, respectively. Thermal history modelling indicates relatively high cooling rates (2–3 °C Ma^{-1}) throughout Permian to early Jurassic times. Since the Jurassic, samples from coastal areas have remained close to the surface and were reheated to 30–50 °C during sedimentary burial in the Cretaceous. Inland samples experienced lesser amounts of Permo-Triassic exhumation, continued to cool slowly (<1 °C Ma^{-1}) throughout the Jurassic–Cretaceous and did not reach the surface until the Cenozoic. Both fission track and (U–Th)/He ages are offset across faults, highlighting the importance of fault activity throughout the Mesozoic. In combination with previously published results, the new data suggest that the geomorphological evolution of southwestern Norway is closely connected to rift- and post-rift tectonics related to North Sea and North Atlantic rifting. The topographic relief was most likely repeatedly rejuvenated during periods of tectonic activity.

The last orogeny to affect southwestern Norway was the Caledonian orogeny during Silurian to earliest Devonian times. The Caledonian orogen was a major continent–continent collision zone and has been envisioned as an ancient analogue for the Himalayas (e.g. Streule *et al.* 2010; Andersen 2011; Gee *et al.* 2011). Thus, peak elevations of several thousand metres (*c.* 8 km?) in the earliest Devonian can be assumed. Continental collision was rapidly followed by extensional collapse, first through ductile and later through brittle modes of deformation (e.g. Eide *et al.* 1997; Andersen *et al.* 1999; Fossen 2000, 2010). Since the early Devonian, southwestern Norway was predominantly affected by extension, resulting in rifting in the North Sea and culminating in the opening of the North Atlantic in the Palaeogene (e.g. Doré *et al.* 1999). Thus the former orogen was transformed into today's inactive North Sea rift system and North Atlantic passive continental margin. However, the details of this transformation, the timing of tectonic events and the evolution of the landscape are still poorly constrained.

Today's landscape in southwestern Norway is characterized by high mountain peaks, vast highland plateaux and deeply incised fjords. In particular, the generally high elevation of the interior of southern Norway is still an enigma and has incited heated debates in the last few years (Lidmar-Bergström & Bonow 2009; Nielsen *et al.* 2009*a*, *b*, 2010*a*, *b*; Chalmers *et al.* 2010; Gabrielsen *et al.* 2010*a*, *b*). Two end-member models suggest the elevated topography to be (a) a remnant of the Caledonian orogen (the ICE hypothesis; Nielsen *et al.* 2009*b*) or (b) the result of Cenozoic tectonic uplift (the peneplanation-uplift model; e.g. reviews by Lidmar-Bergström *et al.* 2000; Gabrielsen *et al.* 2010*a*). The ICE hypothesis assumes that the Devonian orogenic collapse was incomplete, thus allowing for a remnant orogenic root to persist under southern Norway and to potentially support an elevated topography that was slowly eroded to today's level (Nielsen *et al.* 2009*b*). The peneplanation-uplift model, on the other hand, suggests complete orogenic collapse with peneplanation during the Mesozoic followed by renewed tectonic uplift in

From: Corfu, F., Gasser, D. & Chew, D. M. (eds) *New Perspectives on the Caledonides of Scandinavia and Related Areas*. Geological Society, London, Special Publications, **390**, http://dx.doi.org/10.1144/SP390.27

the Cenozoic (e.g. Lidmar-Bergström *et al.* 2000; Gabrielsen *et al.* 2010*a*).

Alternatively, Osmundsen & Redfield (2011) recently observed that the escarpment height along passive continental margins is directly related to crustal thinning gradients established during rifting. They conclude that the rift geometry to a large extent pre-determines the topography of a passive margin, and that this effect lasts long after rifting has ceased. Is the high-elevation topography of southwestern Norway thus essentially Caledonian or is it young (Cenozoic) or created by loading effects on a strongly fractured crust during Permian and Mesozoic rifting?

In the absence of preserved post-Devonian sediments onshore southern Norway, the dating and quantification of periods of uplift relies strongly on indirect methods such as correlation with the offshore sedimentary record and interpretation of onshore erosional surfaces (e.g. Riis 1996; Lidmar-Bergström *et al.* 2000). Currently, the only methods to date vertical movements in the upper crust directly are low-temperature thermochronological methods such as fission track and (U–Th)/He analyses. In this contribution, we discuss the post-Caledonian tectonic history of the area from a low-temperature thermochronological perspective, with a focus on regional and temporal changes in cooling rates during the Mesozoic and Cenozoic as well as the effect of fault reactivation on the distribution of apatite fission track and (U–Th)/He ages.

Previous studies

The pioneers of fission track dating in southwestern Norway were Andriessen & Bos (1986), who concentrated on a geographically small area between innermost Eidfjord and Hardangerjøkulen (Fig. 1). Zircon fission track ages between 320 and 290 Ma and apatite fission track ages between 170 and 110 Ma indicate cooling through the effective closure temperatures of the zircon (*c.* 220 °C) and apatite (*c.* 110 °C) fission track systems in Carboniferous to early Permian and late Jurassic to early Cretaceous times, respectively. Based on the fission track data and previously published K/Ar and Rb/Sr biotite ages (Priem *et al.* 1976), Andriessen & Bos (1986) concluded (a) that initial uplift following the Caledonian orogeny was fast, in the order of 100 m Ma^{-1}, but uplift slowed considerably around late Carboniferous to early Permian times to about 20 m Ma^{-1} and (b) that in total a crustal section of *c.* 13 km has been removed since the end of the Caledonian orogeny.

Nearly a decade later, Rohrman *et al.* (1995) presented the first regionally extensive fission track study with widely spaced samples covering all of southern Norway. Generally, the apatite fission track ages range from *c.* 250 to 100 Ma. Rohrman *et al.* (1995) described the distribution of fission track ages as a domal pattern with the oldest ages (>150 Ma) along the coast and at high elevations inland and young ages (<120 Ma) at low elevations inland. Based on thermal history modelling of fission track ages and track length distributions, they identified two periods of increased uplift in Triassic to Jurassic (<220 Ma) and late Palaeogene to Neogene (<30 Ma) times, respectively, separated by a period of little or no uplift during the Cretaceous to middle Palaeogene. Between 1.3 and 3.5 km of crustal material were removed during Triassic–Jurassic uplift and *c.* 1.5–2.5 km were eroded during the Cenozoic event. The increased erosion rates in the Triassic and Jurassic were attributed to rifting in the North Sea, causing rift flank uplift and base level lowering with associated rift flank erosion. A domal-style regional tectonic uplift is given as the cause of the increased erosion rates during the late Palaeogene and Neogene and the domal distribution of fission track ages. The cause of such a tectonic event remains uncertain.

While Rohrman *et al.* (1995) assumed that all of southern Norway has behaved as a single coherent block since the Caledonian orogeny with no significant post-Permian fault movements, later thermochronological studies came to different conclusions. Redfield *et al.* (2004, 2005) documented that fission track ages are offset across faults of the Møre–Trøndelag Fault Complex and fault-bound blocks have distinctly different exhumation histories from their neighbours. Redfield *et al.* (2004, 2005) suggest that the distribution of fission track ages can be explained by a flexed lithosphere with an uplifted core inboard of a down-faulted retreating scarp rather than the domal uplift of Rohrman *et al.* (1995). This idea later evolved into the crustal taper hypothesis (Osmundsen & Redfield 2011; Redfield & Osmundsen 2013).

A recent regional study by Leighton (2007) covers the area south of the Sognefjorden, with additional samples from Jotunheimen. The sampling sites are mostly widely spaced with a number of detailed vertical and tunnel profiles. Apatite fission track ages range from 280 to 110 Ma. In accordance with Redfield *et al.* (2004, 2005), Leighton (2007) found that the distribution of fission track ages is structurally controlled with large age differences across major fault systems and distinctly different exhumation histories between structurally separated crustal blocks. Similar observations from northern Norway (Hendriks 2003; Hendriks *et al.* 2010) show that large areas of Norway were subjected to fault reactivation during the Mesozoic.

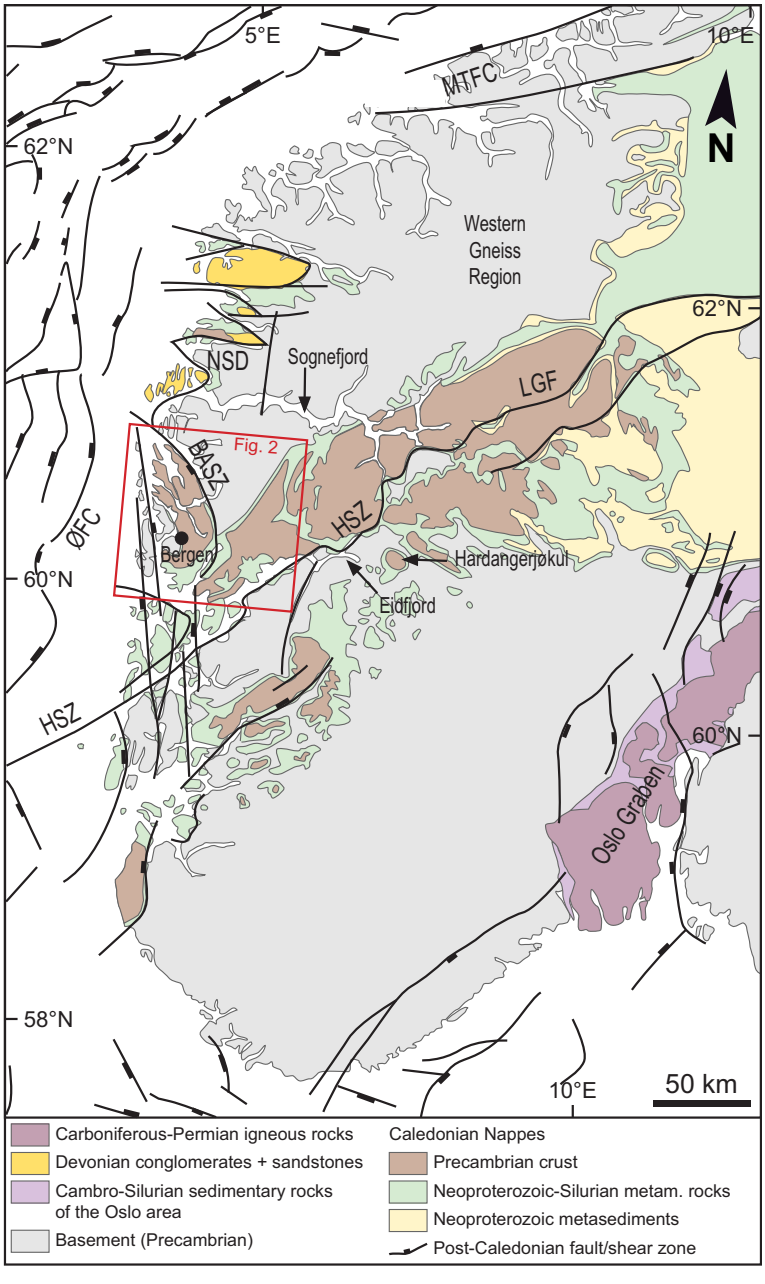

Fig. 1. Simplified geological map of southern Norway, showing the study area (red box) and major fault systems (black). BASZ, Bergen Arc Shear Zone; HSZ, Hardangerfjord Shear Zone; LGF, Lærdal–Gjende Fault Complex; MTFC, Møre–Trøndelag Fault Complex; NSD, Nordfjord–Sogn Detachment Zone; ØFC, Øygarden Fault Complex.

Strong evidence for post-Caledonian faulting onshore southwestern Norway also comes from other geochronological methods. Permian and late Jurassic to early Cretaceous activity has been palaeomagnetically dated along faults related to the Nordfjord–Sogn Detachment Zone and the Lærdal–Gjende Fault Complex (Fig. 1; Torsvik *et al.* 1992; Andersen *et al.* 1999). These ages are supported by K/Ar dating of breccias within the Nordfjord–Sogn Detachment Zone (Eide *et al.*

1997). New K/Ar illite ages of fault gouges from southwestern Norway, including two samples from the Lærdal–Gjende Fault, indicate fault movements in early Carboniferous, Permian, late Triassic to early Jurassic and Cretaceous to earliest Palaeogene times respectively (Ksienzyk 2012; Ksienzyk *et al.* 2012). Additionally, Jurassic sediments discovered during construction of a subsea tunnel west of Bergen are preserved in a fault zone and their internal layering is disrupted by faults, proving beyond doubt that some faults were active at least until the late Jurassic (Fossen *et al.* 1997).

Samples and analytical methods

Sample locations are shown in Figure 2 and given in Table 1. Approximately 4–6 kg of rock were crushed for each sample to grain sizes <315 μm, and apatite and zircon were separated by standard mineral separation techniques, that is Wilfley table, Frantz magnetic separator and heavy liquids. The apatite separates were sieved and only apatites >100 μm were further prepared for analysis.

Fission track analyses were performed at the Department of Earth Science, University of Bergen (Norway). Uranium contents were determined using the external detector method (Gleadow 1981). To determine the apatite fission track ages, the zeta calibration approach was applied (Hurford & Green 1983). Analytical details are included in the caption of Table 1.

(U–Th)/He analyses were carried out at the Geoscience Centre, University of Göttingen (Germany). Single apatite and zircon crystals were handpicked from each sample using binocular and

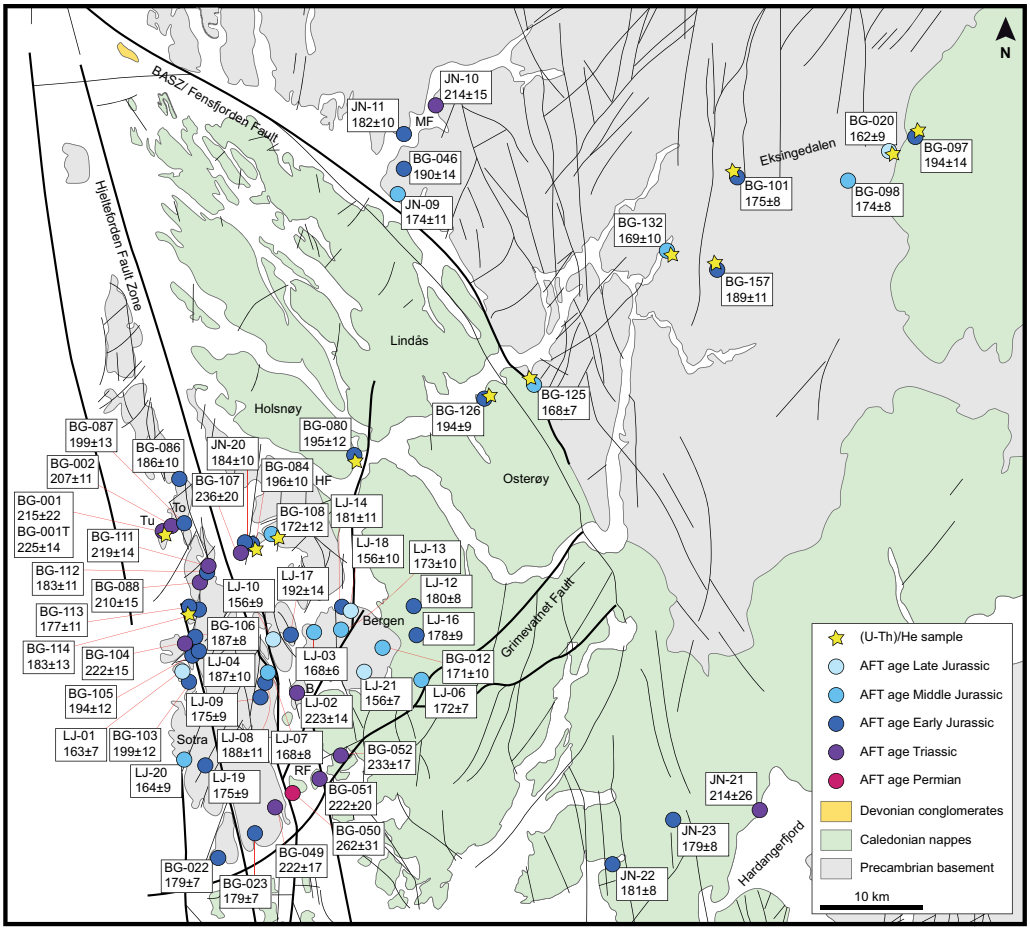

Fig. 2. Simplified geological map of the study area, showing sample locations and apatite fission track ages, as well as place names discussed in the text. Errors are given at their 1σ level. Selected faults are shown in black. B, Bjorøy; BASZ, Bergen Arc Shear Zone; HF, Herdlefjorden; MF, Masfjorden; RF, Raunefjorden; To Toftøy; Tu, Turøy.

petrographic microscopes. The selected crystals all show well-defined (ideally euhedral) external morphologies and are (as much as possible) free of cracks and inclusions. However, chemical zonation of the crystals, which is commonly observed in the apatite fission track samples from the study area, could not be monitored during the selection process. The analytical procedures are detailed in the caption of Table 2. An alpha-ejection correction (F_T correction) was applied to all raw (U–Th)/He ages, following the procedures of Farley *et al.* (1996) and Hourigan *et al.* (2005).

Thermal history modelling

Thermal history modelling was performed with HeFTy 1.8.0 (Ketcham 2005). For modelling of the apatite age and track length data, the annealing model of Ketcham *et al.* (2007*b*) was chosen. Etch pit diameters (Dpar) were used as the kinetic parameter (Donelick *et al.* 2005). Confined track lengths were corrected by *c*-axis projection (Ketcham *et al.* 2007*a*). For modelling of (U–Th)/He data, the radiation damage accumulation and annealing model (RDAAM) of Flowers *et al.* (2009) was used. Weighted mean paths were used to compare time–temperature histories between samples. During modelling, the following external constraints were considered:

Start: zircon fission track ages range from 320 to 230 Ma in the study area (Andriessen & Bos 1986; Leighton 2007; R. Kumar, pers. comm. 2010). Assuming an effective closure temperature of the zircon fission track system at appropriate cooling rates (1–10 °C Ma^{-1}) of *c.* 240–200 °C (Bernet 2009), the starting constraint for all models was set to 320–230 Ma and 240–200 °C.

End: present-day monthly surface temperatures vary throughout the year from *c.* 0 to 15 °C in coastal areas and at low elevations along the large fjords, from *c.* −3 to 12 °C at intermediate elevations (around 500 m) inland and from *c.* −5 to 10 °C at high elevations (>1000 m) inland. These temperature ranges were used as the end constraint, depending on the sample location.

Jurassic exhumation and subsequent reburial: middle to late Jurassic sediments were discovered in a subsea tunnel close to Bjorøy, an island SW of Bergen (Fossen *et al.* 1997). This indicates that the basement of this coastal area was already at (or at least near) the surface in the Jurassic and was subsequently buried under sediments during the Jurassic and the Cretaceous. The age of the Bjorøy Formation is given as Oxfordian, based on its dinocyst assemblage (Fossen *et al.* 1997). Vitrinite reflectance values of 0.28–0.29 Ro from coal fragments recovered from the Bjorøy Formation indicate maximum temperatures during reburial of no more than 50 °C. The sediments encountered in the tunnel are preserved within a fault zone. However, seismic data indicate that Jurassic sediments of 50–60 m thickness may also occur above the tunnel in the Vatlestraumen area (Fossen *et al.* 1997). No sediments are preserved onshore on either the Bjorøy or the mainland side, but are mapped as gently west-dipping strata on offshore seismic lines that project eastwards above Sotra and Øygarden (Fossen 1998). It is uncertain exactly how much basement was eroded in addition to the sedimentary cover. Assuming a maximum post-Jurassic throw of 1 km along the faults downfaulting the Jurassic sediments in Vatlestraumen gives the following constraints for the modelling: (a) Jurassic surface exposure at 170–150 Ma and 0–40 °C (surface temperature + maximum 1 km eroded basement); (b) post-Jurassic reburial from 150 to 0 Ma and 0–80 °C (maximum temperatures of 50 °C + maximum 1 km eroded basement). The extent of a Jurassic sediment cover is unknown. Since the sediments encountered in the Bjorøy Tunnel were interpreted as a coastal facies (Fossen *et al.* 1997), it can be assumed that they did not extent very far inland. However, rising sea-levels during the Cretaceous might have caused significantly larger parts of Norway to be covered with sediments.

Thermochronology

Apatite fission track ages

Fifty-nine apatite samples were analysed by the fission track method. The results are shown in Figures 2 and 3 and are presented in Table 1. The obtained ages range from late Permian to late Jurassic (262–156 Ma), but the majority of samples gave early to middle Jurassic ages (200–160 Ma). However, two areas with predominantly older (Triassic) ages are located around northwestern Sotra, Turøy and Toftøy and in a roughly triangular area around Bjorøy and Raunefjorden, including the islands in the fjord and adjacent areas on Sotra and the mainland (Fig. 2). The ages seem to decrease slightly with distance from the coast, although the scatter is considerable and the correlation hardly significant (Fig. 3a). However, while Jurassic ages occur both inland and at the coast, Triassic ages seem to be mostly restricted to areas west of Bergen. No correlation between age and elevation could be observed and some of the oldest ages were found at sea-level (Fig. 3b). Locally, large age differences (30–50 Ma) occur over short distances (0.5–4 km) between samples that were collected from the same elevation. Some of these age offsets

Table 1. *Apatite fission track data*

Sample no.	UTM (zone 32N)		Elevation (m)	*n* (G)	Spontaneous		Induced		Dosimeter		P(χ^2) (%)	Disp.	U (ppm)	Dpar (μm)	±1σ (μm)	Age* (Ma)	±1σ (Ma)	Measured		*c*-Axis projection		*n* (TL)
	Easting	Northing			ρ_s	N_s	ρ_i	N_i	ρ_d	N_d								MTL (μm)	±1σ (μm)	MTL (μm)	±1σ (μm)	
BG-001	275663	6708926	20	18	6.957	232	7.197	240	18.906	35438	48.97	0.13	6.21	1.31	0.05	215	22					
BG-001T	275663	6708926	20	20	6.572	529	6.770	545	20.232	31968	93.89	0.00	5.47	1.34	0.10	225	14	12.18†	2.71	13.68	1.43	100
BG-002	276360	6709180	15	20	24.098	706	25.395	744	18.961	35438	58.76	0.02	19.14	1.22	0.10	207	11	11.89	1.78	13.29	1.14	100
BG-012	297001	6697263	480	22	12.881	790	13.924	854	16.046	34038	19.58	0.12	14.30	1.23	0.09	171	10					
BG-020	346594	6746068	515	21	8.619	783	11.338	1030	18.348	26276	29.83	0.10	9.01	1.34	0.11	162	9	12.33	1.39	13.55	1.05	102
BG-022	280858	6676689	20	21	15.433	1282	18.767	1559	18.852	35438	93.91	0.00	15.42	1.21	0.07	179	7					
BG-023	284442	6679078	45	19	27.461	1988	33.277	2409	18.798	35438	25.34	0.05	25.92	1.16	0.07	179	7	10.73	1.51	12.48	0.99	134
BG-046	299058	6744099	375	22	3.829	381	4.683	466	20.194	38918	35.39	0.10	3.43	1.58	0.10	190	14					
BG-049	286381	6681627	20	19	7.924	381	7.696	370	18.788	31968	90.12	0.00	5.96	1.34	0.06	222	17					
BG-050	288119	6683188	5	24	2.952	166	2.418	136	18.744	31968	99.99	0.00	1.93	1.56	0.09	262	31					
BG-051	290807	6684334	5	26	3.803	313	3.694	304	18.700	31968	52.93	0.16	3.35	1.26	0.08	222	20					
BG-052	292830	6686866	10	21	5.461	398	5.022	366	18.656	31968	98.40	0.00	3.85	1.51	0.10	233	17					
BG-080	294167	6716069	20	20	7.809	508	9.331	607	20.226	26276	95.61	0.00	6.77	1.47	0.10	195	12	13.00	1.77	14.11	0.96	70
BG-084	284078	6707426	15	20	7.751	792	9.375	958	20.615	26276	99.24	0.00	6.46	1.26	0.08	196	10	12.96†	1.19	14.03	0.79	100
BG-086	277004	6713728	25	20	10.618	714	13.235	890	20.144	31968	34.77	0.03	9.01	1.29	0.07	186	10					
BG-087	277540	6709367	20	18	10.738	451	12.500	525	20.188	31968	89.57	0.00	10.36	1.30	0.11	199	13					
BG-088	279042	6703502	10	20	7.831	500	8.520	544	20.013	31968	17.77	0.11	7.04	1.23	0.08	210	15					
BG-097	349151	6747434	580	28	4.297	413	4.672	449	18.283	26276	53.44	0.07	3.81	1.33	0.14	194	14	12.23†	2.23	13.58	1.41	100
BG-098	342397	6742607	415	28	20.215	1097	24.803	1346	18.477	26276	64.68	0.07	21.46	1.18	0.08	174	8					
BG-101	331731	6743408	270	23	12.442	1285	15.579	1609	18.866	26276	35.10	0.06	11.61	1.37	0.10	175	8	11.97	1.81	13.45	1.08	109
BG-103	277958	6693864	5	26	16.252	542	18.172	606	19.313	31968	85.62	0.01	14.32	1.12	0.08	199	12					
BG-104	277580	6697598	35	20	10.632	485	10.589	483	19.269	31968	83.14	0.01	9.23	1.23	0.06	222	15					
BG-105	278303	6696425	20	21	9.877	728	11.207	826	19.225	31968	8.61	0.15	8.76	1.25	0.10	194	12					
BG-106	278609	6698237	45	20	26.268	1332	31.080	1576	19.181	31968	93.18	0.00	22.42	1.28	0.09	187	8	12.50	1.58	13.78	1.05	104
BG-107	283082	6706548	5	20	6.371	307	6.143	296	19.882	31968	56.97	0.04	4.36	1.34	0.07	236	20					
BG-108	286071	6708245	25	20	6.689	367	8.894	488	19.794	31968	57.82	0.03	6.51	1.23	0.08	172	12	12.56†	1.36	13.77	0.91	100
BG-111	279878	6705213	15	23	15.817	550	16.507	574	19.926	31968	99.94	0.00	12.50	1.18	0.06	219	14					
BG-112	279742	6704573	15	21	8.831	486	11.120	612	19.969	31968	94.34	0.00	8.40	1.14	0.05	183	11					
BG-113	278030	6701193	20	21	11.368	559	14.194	698	19.138	31968	37.24	0.05	12.32	1.33	0.08	177	11	11.81	2.17	13.34	1.21	100
BG-114	278911	6700897	40	18	9.968	405	12.010	4.88	19.094	31968	58.13	0.06	10.62	1.29	0.08	183	13					
BG-125	311805	6722974	55	22	13.265	1070	18.014	1453	19.773	26276	87.45	0.00	13.02	1.30	0.07	168	7	11.95	1.79	13.34	1.25	98
BG-126	306994	6721539	20	22	11.583	954	13.757	1133	19.967	26276	60.46	0.02	10.84	1.27	0.10	194	9	12.41	1.39	13.64	0.89	112
BG-132	324811	6736077	20	21	8.195	521	10.774	685	19.254	26276	64.75	0.03	9.31	1.30	0.13	169	10	11.85	1.26	13.23	1.03	22
BG-157	329744	6734251	1100	20	6.068	624	6.982	718	18.931	26276	57.58	0.00	5.41	1.25	0.09	189	11	13.24†	1.29	14.24	0.96	100

JN-09	298375‡	6741625‡	<50	20	12.249	815	16.398	1091	20.162	38918	1.58	0.18	13.99	1.20	0.09	174	11					
JN-10	302125‡	6750250‡	<20	21	10.481	850	12.084	980	20.259	38918	1.56	0.20	8.75	1.29	0.09	214	15					
JN-11	299000‡	6747500‡	<10	21	8.069	722	10.304	922	20.226	38918	83.49	0.01	7.51	1.20	0.08	182	10					
JN-20	283500‡	6707500‡	<10	20	10.474	698	12.484	832	19.015	35438	68.94	0.02	9.11	1.09	0.07	184	10					
JN-21	334000‡	6681375‡	<20	9	9.446	210	9.536	212	18.744	35438	11.80	0.19	7.18	1.61	0.08	214	26					
JN-22	319500‡	6676000‡	<20	21	16.560	1168	19.594	1382	18.581	35438	81.70	0.00	15.73	1.24	0.09	181	8					
JN-23	325500‡	6680375‡	<100	24	20.769	1259	25.108	1522	18.635	35438	16.17	0.08	20.77	1.35	0.11	179	8					
LJ-01	277232	6694478	15	22	20.830	1241	25.076	1494	17.026	34038	45.96	0.03	22.14	1.18	0.09	163	7					
LJ-02	288521	6692765	65	19	11.706	625	10.226	546	16.999	34038	78.84	0.01	9.08	1.17	0.07	223	14					
LJ-03	290210	6698727	55	21	19.203	1530	22.341	1780	16.973	34038	41.30	0.02	19.09	1.16	0.08	168	6					
LJ-04	278967	6696939	40	20	13.536	1097	14.387	1166	16.946	34038	7.03	0.12	12.14	1.20	0.10	187	10					
LJ-06	300727	6694083	80	20	17.294	1590	19.523	1795	16.867	34038	70.95	0.01	16.53	1.36	0.08	172	7					
LJ-07	285722	6694858	75	22	16.443	1302	19.019	1506	16.841	34038	6.35	0.10	16.49	1.27	0.07	168	8					
LJ-08	285428	6693772	235	26	11.655	598	11.986	615	16.814	34038	95.35	0.00	11.22	1.21	0.10	188	11					
LJ-09	285654	6693103	305	20	22.106	897	24.373	989	16.788	34038	37.81	0.02	20.59	1.12	0.06	175	9					
LJ-10	286260	6698065	35	24	12.616	791	15.773	989	16.761	34038	32.40	0.11	15.44	1.13	0.11	156	9					
LJ-12	299956	6701315	475	20	29.485	1705	31.525	1823	16.708	34038	9.92	0.09	26.78	1.21	0.10	180	8					
LJ-13	292843	6698941	395	20	17.014	791	18.993	883	16.655	34038	10.67	0.12	16.85	1.18	0.07	173	10					
LJ-14	292981	6701212	140	21	11.707	918	12.332	967	16.364	34038	4.21	0.16	11.98	1.21	0.08	181	11					
LJ-16	300303	6698446	425	20	22.194	841	23.407	887	16.285	34038	64.09	0.02	21.71	1.24	0.08	178	9					
LJ-17	287901	6698499	35	22	7.646	430	7.433	418	16.258	34038	71.54	0.01	7.72	1.21	0.13	192	14					
LJ-18	293861	6700793	10	19	29.678	1045	35.046	12.34	16.205	34038	0.30	0.19	32.38	1.24	0.08	156	10	11.86	1.21	13.24	0.83	106
LJ-19	279551	6685752	35	20	16.045	818	17.163	875	16.179	34038	49.00	0.05	17.03	1.24	0.07	175	9					
LJ-20	277479	6686254	5	20	16.866	737	19.085	834	16.126	34038	77.97	0.00	18.55	1.12	0.10	164	9					
LJ-21	295092	6694748	80	20	22.114	1171	26.288	1392	16.073	34038	59.73	0.01	22.44	1.18	0.08	156	7					

MTL, mean track length; *n* (G), number of dated grains; *n* (TL), number of measured track lengths; $N_{s,\,i,\,d}$, number of tracks counted; $\rho_{s,\,i,\,d}$, track densities in 1×10^5 tracks cm^{-2}; P(χ^2), p-value of the chi-square age homogeneity test (Galbraith 2005)

*Central age.

†Irradiated with ^{252}Cf to increase number of confined tracks.

‡Approximate locations (estimated from map); all other locations are GPS positions.

Sample preparation: the apatites were embedded in epoxy, then ground and polished to approximately half the grain thickness to expose internal crystal surfaces. The apatites were etched in 5 M nitric acid for 20 s at 20 $\pm$ 0.5 °C to reveal spontaneous fission tracks. Irradiation of the samples was carried out at the FRM II research reactor at the Technical University Munich (Germany), using a thermal neutron flux of 1×10^{16} neutrons cm^{-2}. Dosimeter glasses IRMM-540R (15 ppm U) were used to monitor the neutron flux. Mica detectors were etched in 40% hydrofluoric acid at room temperature for 20 minutes to reveal the induced tracks.

Analytical conditions: an Olympus BX51 optical microscope equipped with a computer-driven stage and the FT-Stage software (Dumitru 1993) was used for counting fission tracks at a magnification of 1250× and measuring etch pit diameters (Dpar; Donelick *et al.* 2005) and track lengths at a magnification of 2000×. Five Dpar measurements were carried out on each grain that was counted and three Dpar measurements for each measured track length. Only TinTs (track-in-track) were measured and their angle with the *c*-axis was recorded. Fission track ages were calculated with TrackKey (Dunkl 2002) using a zeta calibration factor of 233.56 $\pm$ 3.27 (Ksienzyk).

Table 2. *(U–Th)/He data*

Sample, aliquot*	Helium†		U^{238}			Th^{232}				Sm			Ejection correction (Ft)‡	Uncorrected He-age (Ma)	Ft-corrected He-age (Ma)	1σ (Ma)	Sphere radius (μm)	Rad.§ (He nmol g^{-1})	Sample average	
	Volume (ncc)	1σ (%)	Mass (ng)	1σ (%)	Concentration (ppm)	Mass (ng)	1σ (%)	Concentration (ppm)	Th/U ratio	Mass (ng)	1σ (%)	Concentration (ppm)							Age (Ma)	±1σ (Ma)
BG-001T, a1	0.231	2.12	0.008	5.91	2.43	0.009	4.41	2.61	1.07	0.312	9.32	92.96	0.738	148.25	200.87	12.23	42	3.1	154	34
BG-001T, a2	0.189	2.10	0.008	6.13	1.22	0.008	4.63	1.25	1.03	0.398	9.19	63.14	0.776	121.24	156.17	9.12	49	1.3		
BG-001T, a3	0.183	2.23	0.006	8.02	1.90	0.018	3.36	5.99	3.15	0.344	9.00	114.15	0.762	117.24	153.84	9.07	44	2.7		
BG-001T, a4	0.129	2.38	0.004	12.77	1.26	0.016	3.52	5.35	4.25	0.416	8.86	143.33	0.754	98.69	130.85	8.87	42	2.0		
BG-001T, a5	1.238	1.73	0.036	2.20	7.10	0.122	2.54	23.92	3.37	0.896	8.78	175.29	0.781	139.97	179.23	7.33	48	10.8		
BG-001T, a6	0.062	2.96	0.004	12.51	1.29	0.003	9.08	0.91	0.71	0.269	8.60	91.02	0.736	77.25	104.95	9.42	41	0.9		
BG-020, a1	0.161	2.18	0.011	4.61	2.95	0.012	3.06	3.38	1.15	0.251	12.15	70.28	0.820	85.96	104.85	5.15	85	2.0	121	17
BG-020, a2	0.067	2.85	0.004	12.24	1.75	0.005	4.17	2.22	1.27	0.159	12.41	76.96	0.768	92.08	119.83	10.59	47	1.5		
BG-020, a3	0.243	2.03	0.009	5.13	1.66	0.016	2.87	2.85	1.72	0.941	12.64	164.18	0.793	95.01	119.77	7.62	52	1.9		
BG-020, a4	0.595	1.84	0.024	2.62	2.27	0.031	2.63	2.94	1.30	1.161	12.91	110.99	0.802	120.55	150.28	7.34	55	2.5		
BG-020, a5	0.117	2.50	0.007	6.96	1.25	0.007	3.56	1.32	1.06	0.381	13.82	71.61	0.752	84.49	112.41	7.93	44	1.0		
BG-080, a1	0.097	2.48	0.006	8.43	4.68	0.009	3.34	7.47	1.59	0.191	7.83	161.93	0.671	87.45	130.42	9.82	32	3.7	109	15
BG-080, a2	0.096	2.46	0.006	7.90	2.15	0.001	8.20	0.42	0.19	0.462	7.82	167.69	0.673	79.10	117.61	9.06	34	1.6		
BG-080, a3	0.090	2.60	0.006	8.52	2.74	0.003	5.32	1.31	0.48	0.529	7.78	256.16	0.624	69.50	111.42	9.17	27	1.9		
BG-080, a4	0.094	2.55	0.006	8.41	2.25	0.000	15.18	0.18	0.08	0.536	7.77	206.95	0.673	74.56	110.87	8.75	34	1.6		
BG-080, a5	0.104	2.55	0.008	5.86	2.96	0.002	6.30	0.68	0.23	0.743	7.77	268.82	0.675	58.09	86.06	6.12	34	1.7		
BG-080, a6	0.074	2.88	0.005	9.22	3.25	0.001	7.96	0.76	0.23	0.468	7.79	296.37	0.667	65.57	98.35	8.11	33	2.1		
BG-084, a1	0.549	1.78	0.018	3.10	2.59	0.031	2.64	4.38	1.69	0.367	14.43	52.65	0.761	159.03	209.06	9.92	45	3.5	204	32
BG-084, a3	0.540	1.83	0.016	3.31	1.58	0.020	2.78	1.94	1.23	0.290	9.01	27.82	0.769	187.17	243.37	11.26	47	2.3		
BG-084, a4	0.542	1.84	0.020	2.89	1.38	0.043	2.57	3.03	2.20	0.539	9.04	37.80	0.777	129.58	166.72	7.28	48	1.7		
BG-084, a5	0.555	1.80	0.019	3.07	1.58	0.035	2.61	2.82	1.78	0.438	8.99	35.64	0.745	145.72	195.66	9.35	42	2.0		
BG-097, a1	0.291	1.89	0.022	2.76	3.19	0.002	6.41	0.26	0.08	0.065	8.03	9.45	0.806	103.79	128.81	5.55	57	1.9	116	18
BG-097, a2	*0.156*	*2.19*	*0.007*	*6.65*	*3.96*	*0.006*	*3.82*	*3.37*	*0.85*	*0.208*	*7.95*	*119.31*	*0.672*	*127.94*	*190.34*	*13.53*	*33*	*4.0*		
BG-097, a3	0.062	2.86	0.005	9.11	1.04	0.002	6.46	0.41	0.39	0.022	9.15	4.56	0.675	89.28	132.24	12.72	33	0.6		
BG-097, a4	0.536	1.79	0.026	2.62	2.19	0.069	2.50	5.87	2.68	0.101	9.09	8.56	0.806	102.46	127.13	4.91	55	2.0		
BG-097, a5	0.318	1.92	0.017	2.80	5.41	0.070	2.50	22.46	4.15	0.132	9.02	42.14	0.805	75.43	93.71	3.69	53	4.5		
BG-097, a7	0.253	1.94	0.024	2.52	10.83	0.008	3.39	3.70	0.34	0.045	9.05	19.99	0.785	78.89	100.49	4.40	26	5.1		
BG-101, a1	1.146	1.71	0.047	2.06	6.76	0.064	2.51	9.23	1.37	0.204	10.51	29.56	0.784	148.30	189.14	7.56	50	7.4	210	36
BG-101, a2	1.573	1.70	0.076	1.92	8.35	0.051	2.54	5.61	0.67	0.289	10.75	31.61	0.793	141.70	178.63	6.94	53	7.7		
BG-101, a3	0.806	1.76	0.026	2.50	5.60	0.022	2.73	4.86	0.87	0.150	11.07	32.44	0.734	202.55	276.06	13.27	41	7.8		
BG-101, a4	0.850	1.78	0.034	2.26	6.54	0.036	2.60	6.91	1.06	0.340	11.19	65.50	0.791	153.94	194.64	7.88	73	7.3		
BG-101, a5	0.895	1.74	0.040	2.14	8.16	0.030	2.64	6.15	0.75	0.271	11.43	55.39	0.777	148.84	191.57	8.00	49	8.2		
BG-101, a6	0.278	2.02	0.011	4.39	4.90	0.010	3.19	4.43	0.91	0.053	11.95	23.69	0.721	165.30	229.24	13.24	39	5.5		
BG-101, a7	0.633	1.78	0.039	2.85	9.68	0.011	3.33	2.68	0.28	0.101	4.58	24.90	0.756	121.99	161.26	7.72	46	7.0		
BG-101, a8	2.344	1.68	0.079	2.10	18.74	0.102	2.48	23.99	1.28	0.262	4.41	61.89	0.760	181.30	238.57	10.24	45	24.7		
BG-101, a9	1.968	1.68	0.070	2.17	19.86	0.094	2.48	26.66	1.34	0.129	4.34	36.75	0.739	172.91	233.96	10.71	41	25.0		
BG-108, a1	1.035	1.71	0.048	2.00	5.36	0.101	2.47	11.12	2.07	0.576	5.60	63.67	0.833	110.51	132.63	4.47	94	5.1	165	22
BG-108, a2	1.919	1.68	0.059	1.93	3.50	0.141	2.45	8.32	2.38	1.117	5.40	65.73	0.845	154.16	182.40	5.85	101	5.0		
BG-108, a3	*3.180*	*1.66*	*0.144*	*1.84*	*6.43*	*1.229*	*2.41*	*55.05*	*8.56*	*2.762*	*5.34*	*123.70*	*0.854*	*57.37*	*67.18*	*2.16*	*112*	*6.4*		
BG-108, a4	0.782	1.75	0.025	2.59	2.93	0.057	2.53	6.61	2.26	0.518	5.49	59.71	0.843	148.44	176.08	6.01	100	4.0		
BG-108, a5	1.007	1.72	0.037	2.21	4.11	0.067	2.51	7.54	1.83	0.759	5.46	85.15	0.825	140.47	170.20	5.99	89	5.0		
BG-113, a1	0.288	1.90	0.024	2.47	5.66	0.027	2.67	6.34	1.12	0.618	5.57	145.11	0.759	66.76	88.00	3.95	45	3.0	162	60
BG-113, a3	0.670	1.77	0.025	3.69	19.12	0.043	2.59	32.21	1.69	0.342	4.25	258.64	0.698	144.10	206.43	11.25	34	22.7		
BG-113, a5	0.212	2.03	0.010	8.50	10.36	0.009	3.60	9.21	0.89	0.170	4.35	175.11	0.655	128.33	195.95	16.17	30	9.8		
BG-113, a6	1.032	2.10	0.038	2.33	20.59	0.090	2.42	49.16	2.39	0.495	10.18	268.82	0.621	133.70	215.17	13.53	43	25.0		

BG-113, a7	0.646	2.25	0.027	3.00	14.04	0.052	3.00	27.39	1.95	0.422	3.33	220.33	0.630	66.46	105.56	6.80	43	15.0		
BG-113, a8	*0.830*	*2.16*	*0.024*	*2.97*	*11.29*	*0.054*	*2.43*	*25.50*	*2.26*	*0.389*	*10.24*	*185.13*	*0.672*	*171.42*	*254.95*	*14.66*	*49*	*17.6*		
BG-125, a1	0.719	1.77	0.049	2.04	11.64	0.033	2.62	8.00	0.69	0.183	9.03	43.87	0.776	102.10	131.53	5.47	49	7.7	133	14
BG-125, a2	1.910	1.70	0.111	1.86	10.59	0.049	2.55	4.63	0.44	0.132	9.40	12.58	0.829	126.71	152.93	5.33	88	8.1		
BG-125, a3	0.636	1.83	0.048	2.05	9.15	0.017	2.84	3.28	0.36	0.093	9.62	17.50	0.794	98.02	123.43	4.96	54	5.4		
BG-125, a4	0.168	2.20	0.014	3.65	3.70	0.004	4.40	1.02	0.28	0.036	9.83	9.34	0.755	88.53	117.30	6.31	43	1.9		
BG-125, a6	0.588	1.85	0.040	2.15	10.08	0.015	2.91	3.83	0.38	0.084	10.20	21.13	0.780	109.27	140.02	5.91	50	6.6		
BG-126, a1	0.051	3.07	0.005	9.15	3.10	0.000	18.56	0.23	0.07	0.048	7.76	29.67	0.689	76.83	111.47	10.92	35	1.4	126	39
BG-126, a2	0.643	1.79	0.025	2.57	3.24	0.033	2.62	4.35	1.34	0.565	7.81	74.39	0.773	141.99	183.76	7.96	47	3.8		
BG-126, a3	0.068	2.88	0.007	6.61	3.51	0.005	4.13	2.25	0.64	0.079	7.93	38.12	0.709	62.66	88.37	6.50	37	1.5		
BG-126, a4	0.167	2.15	0.010	4.96	2.32	0.001	12.58	0.14	0.06	0.127	7.85	28.61	0.741	118.94	160.54	9.97	41	1.7		
BG-126, a5	0.073	2.82	0.008	5.87	1.72	0.001	9.32	0.20	0.12	0.098	7.97	20.99	0.733	66.00	89.99	6.34	42	0.7		
BG-126, a6	0.074	2.63	0.006	7.45	1.72	0.002	6.66	0.49	0.29	0.096	8.16	26.88	0.675	82.75	122.53	10.06	32	0.9		
BG-132, a1	0.106	2.25	0.007	7.41	1.30	0.007	3.63	1.32	1.02	0.052	8.33	10.39	0.759	101.89	134.15	9.34	45	0.9	152	40
BG-132, a2	0.109	2.39	0.011	4.66	1.11	0.006	3.72	0.65	0.59	0.038	8.58	3.95	0.768	72.17	93.97	5.38	47	0.5		
BG-132, a3	0.314	1.89	0.016	3.35	2.08	0.012	3.04	1.60	0.77	0.029	8.47	3.66	0.779	132.56	170.14	7.99	49	1.8		
BG-132, a4	0.977	1.73	0.063	1.96	2.65	0.036	2.60	1.49	0.56	0.254	8.66	10.64	0.826	108.55	131.37	4.65	63	1.8		
BG-132, a5	0.710	1.78	0.030	2.42	2.54	0.025	2.70	2.05	0.81	0.048	8.73	4.02	0.778	158.53	203.78	8.69	49	2.6		
BG-132, a6	0.450	1.86	0.023	2.69	2.70	0.014	2.97	1.63	0.61	0.031	8.80	3.63	0.755	136.76	181.12	8.52	45	2.3		
BG-157, a1	0.285	2.01	0.014	3.51	1.34	0.008	3.41	0.76	0.57	1.030	9.07	97.75	0.805	95.53	118.66	6.09	56	1.2	109	19
BG-157, a2	0.098	2.54	0.004	11.20	0.50	0.005	4.17	0.56	1.11	0.773	8.97	92.37	0.782	69.18	88.48	6.64	49	0.5		
BG-157, a4	0.099	2.56	0.006	7.37	1.12	0.003	5.08	0.55	0.49	0.454	9.00	81.65	0.754	75.82	100.60	6.92	44	0.8		
BG-157, a5	0.413	1.87	0.019	2.85	1.88	0.008	3.44	0.78	0.41	1.295	9.08	128.97	0.831	108.24	130.19	6.14	65	1.8		
BG-157, a6	*0.437*	*1.90*	*0.013*	*3.89*	*1.98*	*0.008*	*3.46*	*1.14*	*0.58*	*0.928*	*9.13*	*139.02*	*0.798*	*158.16*	*198.20*	*10.33*	*54*	*2.9*		
BG-020, z1	*10.282*	*1.64*	*0.253*	*1.88*		*0.105*	*2.43*		*0.41*	*0.021*	*9.40*		*0.795*	*298.32*	*375.08*	*14.47*	*61*		286	23
BG-020, z3	14.537	1.64	0.517	1.83		0.164	2.42		0.32	0.029	11.74		0.783	212.48	271.44	10.86	57			
BG-020, z4	64.454	1.64	1.901	1.81		0.685	2.41		0.36	0.042	5.24		0.817	253.12	309.97	11.12	68			
BG-020, z5	10.206	1.69	0.394	1.84		0.139	2.42		0.35	0.014	6.83		0.747	194.68	260.74	11.66	48			
BG-020, z6	23.064	1.66	0.791	1.82		0.207	2.41		0.26	0.022	5.70		0.742	223.12	300.77	13.61	47			
BG-113, z2	21.563	2.32	1.133	1.81		0.157	2.42		0.14	0.009	9.35		0.685	150.70	220.12	12.18	38		225	7
BG-113, z3	19.990	1.64	0.970	1.81		0.125	2.42		0.13	0.015	14.27		0.707	163.23	230.97	11.53	41			
BG-113, z4	30.959	1.66	1.386	1.81		0.345	2.41		0.25	0.017	7.74		0.747	172.18	230.39	10.26	48			
BG-113, z5	40.468	1.65	1.840	1.81		0.291	2.41		0.16	0.009	8.26		0.764	172.99	226.43	9.63	52			
BG-113, z6	20.593	1.67	1.070	1.81		0.129	2.42		0.12	0.008	9.87		0.712	152.96	214.91	10.61	42			
BG-125, z1	67.446	1.64	2.643	1.81		0.758	2.41		0.29	0.021	9.09		0.752	194.66	258.95	11.35	49		265	14
BG-125, z3	39.995	1.64	1.375	1.81		0.828	2.41		0.60	0.017	9.59		0.737	207.30	281.18	12.77	47			
BG-125, z4	36.545	1.65	1.422	1.81		0.577	2.41		0.41	0.021	6.67		0.746	191.12	256.26	11.41	48			

Analyses in italics are excluded from further consideration.

*a, apatite; z, zircon.

†Amount of He is given in nano-cubic-cm in standard temperature and pressure.

‡Ejection correction (Ft): correction factor for alpha-ejection (according to Farley *et al.* 1996; Hourigan *et al.* 2005).

§Radiation density.

Uncertainties: uncertainties of He and the radioactive element contents are given as 1σ, in relative error-percent. Uncertainties of the radioactive element concentrations are *c.* 10% (owing to the high uncertainty in the crystal mass estimation). Uncertainty of the single grain age is given as 1σ in Ma, and it includes both the analytical uncertainty and the estimated uncertainty of the Ft correction. Uncertainty of the sample average age is given as 1σ in Ma.

Analytical procedures: single apatite and zircon crystals were hand-picked, photographed and packed in platinum capsules. Crystal dimensions were obtained from the photographs. To determine the ^{4}He content, the platinum capsules with the enclosed crystals were degassed under high vacuum by heating with an infrared diode laser. After purification with an SAES Ti–Zr getter at 450 °C, the extracted gas was analysed with a Hiden triple-filter quadrupole mass spectrometer, equipped with a positive ion counting detector. To ascertain a quantitative helium extraction, re-extraction was performed for every sample. To analyse the ^{238}U, ^{232}Th and Sm contents, the platinum capsules were retrieved after He analysis, the apatites were dissolved in nitric acid and the zircons in hydrofluoric acid. The dissolved crystals were spiked with calibrated ^{230}Th and ^{233}U solutions and analysed by the isotope dilution method on a Perkin Elmer Elan DRC ICP-MS equipped with an APEX micro flow nebulizer.

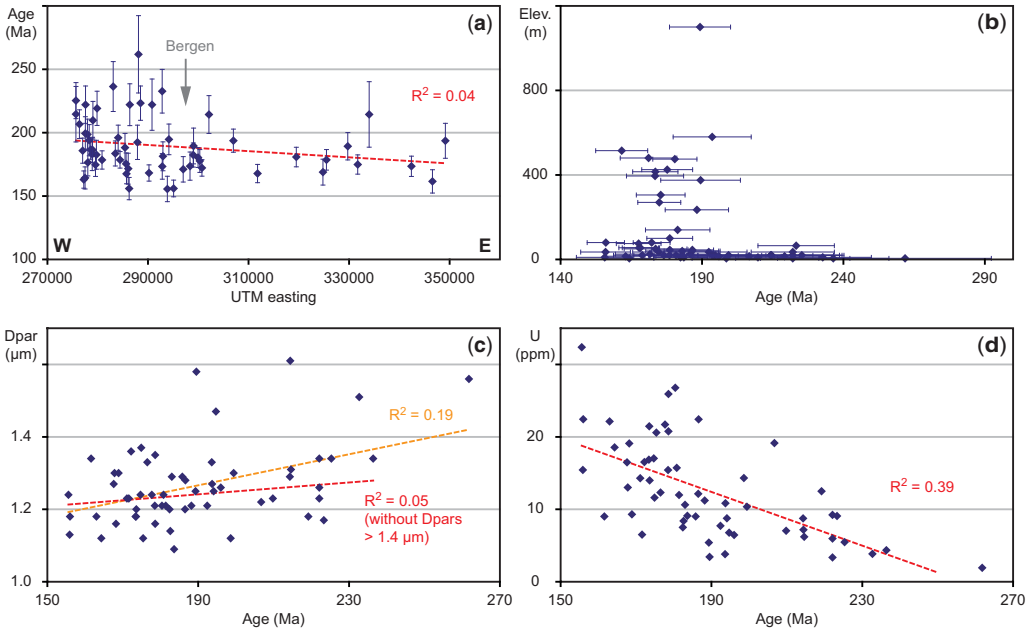

Fig. 3. Apatite fission track ages of 59 samples plotted against (**a**) distance from the coast (approximated by UTM eastings, zone 32N); (**b**) elevation – no correlation with elevation could be observed; (**c**) mean Dpar – the correlation is very weak (orange regression line) and entirely insignificant if the five Dpars >1.4 μm are excluded (red regression line); (**d**) uranium concentration. All error bars are 1σ uncertainties.

occur across mapped faults (particularly strands of the Hjeltefjorden Fault Zone), while others do not appear to coincide with known structures.

The etch pit diameter (Dpar) was measured as a proxy of mineral chemistry and thus the annealing kinetics of the dated apatites (e.g. Donelick *et al.* 2005). The mean Dpars of the samples presented here have a rather narrow range from 1.09 to 1.61 μm, with the majority between 1.1 and 1.4 μm, indicating homogeneous compositions and relatively fluorine-rich mineral chemistries (Fig. 3c). There is no significant correlation between fission track age and Dpar, indicating that differences in mineral chemistry and annealing behaviour cannot be the reason for the observed age differences between samples. Of the five samples with Dpars >1.4 μm, three gave older ages than the surrounding samples with smaller Dpars. The old ages of these three samples (BG-050, BG-052 and JN-21) might be partially explained by a different apatite chemistry. Four samples (JN-09, JN-10, LJ-14, and LJ-18) failed the χ^2-test, which means that the scatter in the single grain ages is larger in these samples than would be expected for a single-age population. For these four samples, the dependence of single grain ages on single grain Dpars was tested, but none of these samples showed any meaningful correlation. Thus even within individual samples, the age scatter cannot be explained by differences in grain chemistry.

The apatite fission track ages presented here show a weak inverse correlation with the mean U-concentrations of the samples (Fig. 3d). Weak to moderately strong inverse correlations between single grain age and single grain U-concentration can also be observed in some of the individual samples. Since, within a sample, the age and U-concentration are not independent variables, both being calculated from the induced track density N_i, some degree of inverse correlation can be inherent in the method (Galbraith 1997). However, radiation-enhanced annealing (REA) has been proposed as an alternative explanation for inverse correlations between U-concentration and age in apatite fission track data (Hendriks & Redfield 2005). We do not suppose that REA had any significant influence on the ages presented here, but its potential impact is discussed below.

Apatite (U–Th)/He ages

Apatite (U–Th)/He analyses were carried out on 12 samples along an 85 km-long profile from Turøy into the Eksingedalen area (Fig. 4; see Fig. 2 for sample locations). Five to nine apatite crystals were dated per sample and the results are presented

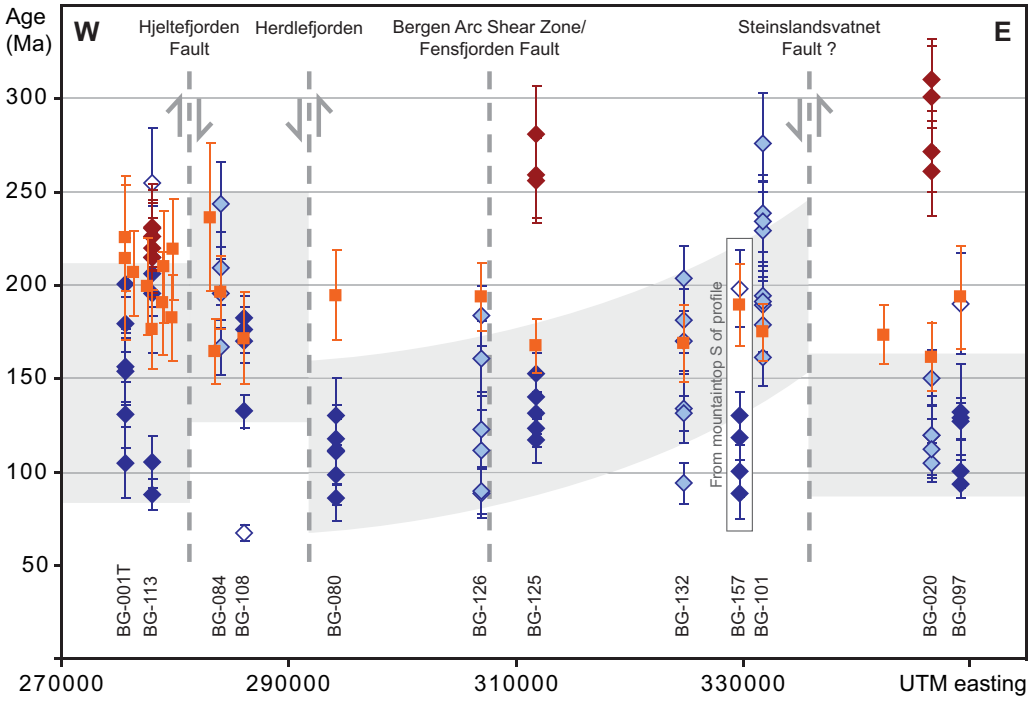

Fig. 4. Apatite and zircon single grain (U–Th)/He ages and fission track ages along a profile from Turøy into the Eksingedalen area. See Figure 2 for samples locations. Sample BG-157 was collected from the top of Storfjelli mountain, *c.* 6 km south of the profile. Filled dark blue diamonds, robust single grain apatite (U–Th)/He ages; filled light blue diamonds, less reliable single grain apatite (U–Th)/He ages (see text for discussion); empty blue diamonds, single grain (U–Th)/He ages that were excluded from further consideration; red diamonds, single grain zircon (U–Th)/He ages; orange squares, fission track ages; grey dashed lines, faults (sense of movement is indicated). Note that error bars are 2σ uncertainties.

in Figure 4 and Table 2. Of altogether 77 single grain analyses, six yielded U or Th concentrations at or below the detection limit, resulting in large errors (1σ errors $>20\%$) and often erroneously old ages ($\gg$400 Ma). Two apatites contained small inclusions (noted during grain selection) and gave significantly older ages than the other aliquots from the respective samples. These eight analyses were discarded and are not included in either figures or tables. Another three analyses are considered to be outliers when compared with the other ages from the respective samples and one apatite (U–Th)/He age was older than the zircon (U–Th)/He ages from the same sample. These analyses are included in Table 2 (italic lettering) and are shown in Figure 4 (open symbols), but they are not included in the calculation of average sample ages or considered during the discussion and interpretation of the data.

The remaining 65 single grain ages range from 276 to 86 Ma, although the majority of ages are early to middle Cretaceous (*c.* 140–90 Ma). Similar to the fission track ages, no correlation between age and elevation was found. The apatite (U–Th)/He ages decrease slightly towards the inland; however, this trend is offset in several places and locally reversed in the central part of the profile. Sample BG-157 from the top of Storfjelli mountain (1100 m), *c.* 6 km south of the profile, gave younger ages than the neighbouring samples. While the sample is shown in Figure 4 (in the box), it should be considered separate from the rest of the profile.

The dispersion of single grain ages within individual samples can be expressed by the standard deviations of the samples, which lie typically around 15% (1σ). However, four samples show significantly greater variability in single grain ages, with the 1σ standard deviation of the sample exceeding 20% (BG-001T: 22%, BG-113: 37%, BG-126: 31%, BG-132: 26%). Flowers & Kelley (2011) suggest rejecting samples where the standard deviation is greater than 20% (1σ) unless the large dispersion can be explained by positive correlations of age with the effective U-concentration (eU) or grain size, or additional data regarding, for

example, the U-distribution within individual apatites, are used to interpret the ages. Accordingly, each individual sample was evaluated as follows. (a) Potential age v. eU and age v. grain size correlations were evaluated. (b) The best-fit-path from the time–temperature model based on only the fission track data from the same sample was used to calculate (U–Th)/He ages for each apatite. Both the modelled ages and the variability of modelled ages within the sample were compared with the measured ages. (c) Inhomogeneities in the U-distributions were qualitatively assessed on the fission track mounts.

Three samples (BG-001T, BG-097 and BG-157) yielded overlapping measured and modelled ages with a similar dispersion of both measured and modelled ages. Samples BG-001T and BG-157 show positive correlations of age with both eU and grain size. Sample BG-097 gave a negative correlation of age with eU and no correlation between age and grain size. All three samples are characterized by mostly homogenous U-distributions. These three samples are considered the most robust fission track-(U–Th)/He data pairs. The fission track and (U–Th)/He data are modelled together and the derived time–temperature histories are taken to be the most reliable.

In another four samples (BG-080, BG-108, BG-113 and BG-125), the modelled and measured ages overlap partially, but only two of these (BG-080 and BG-125) show similar age dispersions in the modelled and measured ages. Both of these have positive correlations between age and eU, and sample BG-125 also has a positive correlation between age and grain size. In sample BG-080, age and grain size are uncorrelated. Sample BG-080 is characterized by a mostly homogeneous U-distribution, whereas in sample BG-125, apatites with inhomogeneous U-distributions dominate. By far the most common geometry is a U-rich core that is slightly larger than half the grain diameter, surrounded by a U-poor rim (Fig. 5). U-concentrations have been obtained for cores and rims of several apatites by the fission track method. While rims gave similar U-concentrations around 4 ppm, cores varied from 18 to 48 ppm. In samples BG-108 and BG-113, the dispersion of the measured ages exceeds that of the modelled ages. Sample BG-113 shows a positive correlation between age and eU and a negative correlation between age and grain size. Sample BG-108 gave a negative correlation between age and eU and a positive correlation between age and grain size. Both of these samples are characterized by relatively homogeneous U-distributions. For these four samples with partially overlapping measured and modelled ages, the fission track and (U–Th)/He data were also modelled together. However, weighted mean paths from the same models based solely on the fission track data are shown for comparison (Fig. 7).

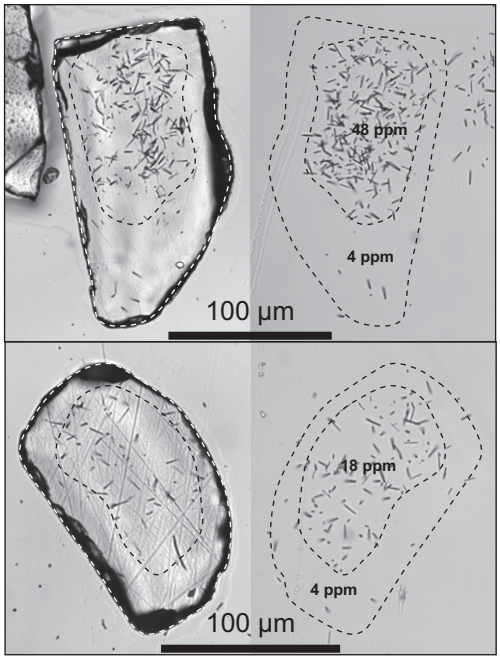

Fig. 5. Zoned apatite grains from sample BG-125. The U concentrations were measured by the fission track method. The rims typically have *c.* 4 ppm U, while the cores are significantly enriched in U with 18–48 ppm. Cores are typically slightly larger than half the grain diameter.

Five samples (BG-020, BG-084, BG-101, BG-126 and BG-132) yielded modelled ages that are significantly older than the measured ages. However, the dispersion of the modelled ages is similar to that of the measured ages with the exception of sample BG-132, where the dispersion of the measured ages significantly exceeds that of the modelled ages. Sample BG-132 shows a positive correlation between age and eU, while all other samples show no correlation between age and eU. Sample BG-126 gave a positive correlation between age and grain size. In the other four samples, age and grain size are uncorrelated (BG-084 and BG-132) or show weak negative correlations (BG-020 and BG-101). All these five samples are characterized by strongly non-homogeneous U-distributions. The effect of non-homogeneous U-distributions on (U–Th)/He ages has been discussed by several authors (Meesters & Dunai 2002; Hourigan *et al.* 2005; Farley *et al.* 2011; Flowers & Kelley 2011; Gautheron *et al.* 2012). The dominant geometry observed in these five samples is U-rich cores surrounded by U-poor

rims, although other geometries (patchy zoning, U-rich rims) do occur sporadically. Such U-depleted rims would generally cause ages to be too old, as observed in all five samples. However, the exact effect on individual (U–Th)/He ages is difficult to assess since no U-distributions were determined for the analysed grains. The (U–Th)/He data from these samples are therefore not used for time–temperature modelling; the models shown in Figures 6 and 7 are based solely on the fission track data from the respective samples. To differentiate the (U–Th)/He ages from these samples that are strongly affected by non-homogeneous U-distributions from the more reliable ages discussed above, they are shown in light blue in Figure 4.

Zircon (U–Th)/He ages

Three samples were chosen for zircon (U–Th)/He dating, from the western end, middle and eastern end of the apatite (U–Th)/He profile (Fig. 4). Between three and five zircon crystals were dated per sample. Out of 13 single grain analyses, one was excluded as an outlier. The remaining 12 ages range from 310 to 215 Ma (Fig. 4, Table 2). The spread of single grain ages within individual samples is smaller than for the apatite ages, ranging from 3 to 8% 1σ sample standard deviations. Other than the apatite (U–Th)/He ages, the zircon ages are increasing with distance from the coast, from late Triassic ages on Sotra, to Permian to Carboniferous ages in Eksingedalen.

The effect of radiation damage

Radiation damage in apatites can potentially affect both the fission track and (U–Th)/He system, especially in old and U-rich samples. Often the (U–Th)/He ages are older than expected from the fission track data and vice versa (e.g. Hendriks & Redfield 2005; Söderlund *et al.* 2005; Green & Duddy 2006; Hansen & Reiners 2006; Kohn *et al.* 2009). As described above, this effect occurs in five of our samples. The question is whether the fission track ages are 'too young' or the (U–Th)/He ages 'too old'. Hendriks & Redfield (2005) suggested REA as a mechanism to produce 'too young' fission track ages in U-rich or very old samples. The same process produces an inverse correlation between U-concentration and age, since U-rich samples are more strongly affected. The concept of REA is highly controversial within the fission track community and has yet to receive further support (Green *et al.* 2006; Green & Duddy 2006; Hendriks & Redfield 2006; Larson *et al.* 2006; Kohn *et al.* 2009). While we do observe an inverse correlation between U-content and fission track age in our data, we would like to point out again that these two variables are dependent, and an inverse correlation between them can be caused by this dependence as well as a so-called 'counting bias' (Galbraith 1997). Apart from this, we consider it unlikely that REA has noticeably affected the apatite fission track ages for a number of reasons. First, the ages presented here are significantly younger than those from cratonic areas in Finland (Hendriks & Redfield 2005) and many samples have relatively low U-contents, thus the accumulated radiation damage should be less extensive. Second, within individual samples, inverse correlations between single grain age and single grain U-concentration were observed in samples with very low U-concentration and a narrow range of U-concentrations just as often as in samples with high and widely variable U-concentrations. This observation is difficult to reconcile with the concept of REA that predicts that U-rich samples should be most strongly affected by REA, thus showing the strongest correlations between U-concentration and age. Third, the sample U-concentrations are uncorrelated with distance from the coast, thus the faint younging trend towards the inland cannot be explained by REA. Finally, while some of the large age differences over short distances that are described above coincide with differences in U-concentrations, many others do not. We conclude therefore that REA might have added to the overall scatter in ages, but the effects are limited, and REA cannot be used to explain the general age distribution.

While radiation damage might facilitate fission track annealing, it also provides traps for He, thus increasing the He-retentivity. This process has gained much wider acceptance and was included into recent annealing models (Shuster *et al.* 2006; Flowers *et al.* 2009). The effect of accumulated radiation damage acting on apatites with a range of different eU-concentrations and grain sizes can produce both widely dispersed (U–Th)/He ages and inversed fission track-(U–Th)/He data pairs, especially in high-eU and slowly cooled samples (Flowers & Kelley 2011).

The effect of accumulated radiation damage has been taken into account by applying the RDAAM model (Flowers *et al.* 2009) to calculate (U–Th)/He ages for each analysed grain based on time–temperature paths derived from the fission track data alone. For seven samples these modelled ages overlap completely, or at least partially, with the measured (U–Th)/He ages. It is therefore reasonable to assume that in these samples the effect of accumulated radiation damage in combination with differences in eU and grain size produced both the relatively old ages and large dispersion of single grain ages. We consider these ages to be geologically meaningful, representing slow cooling

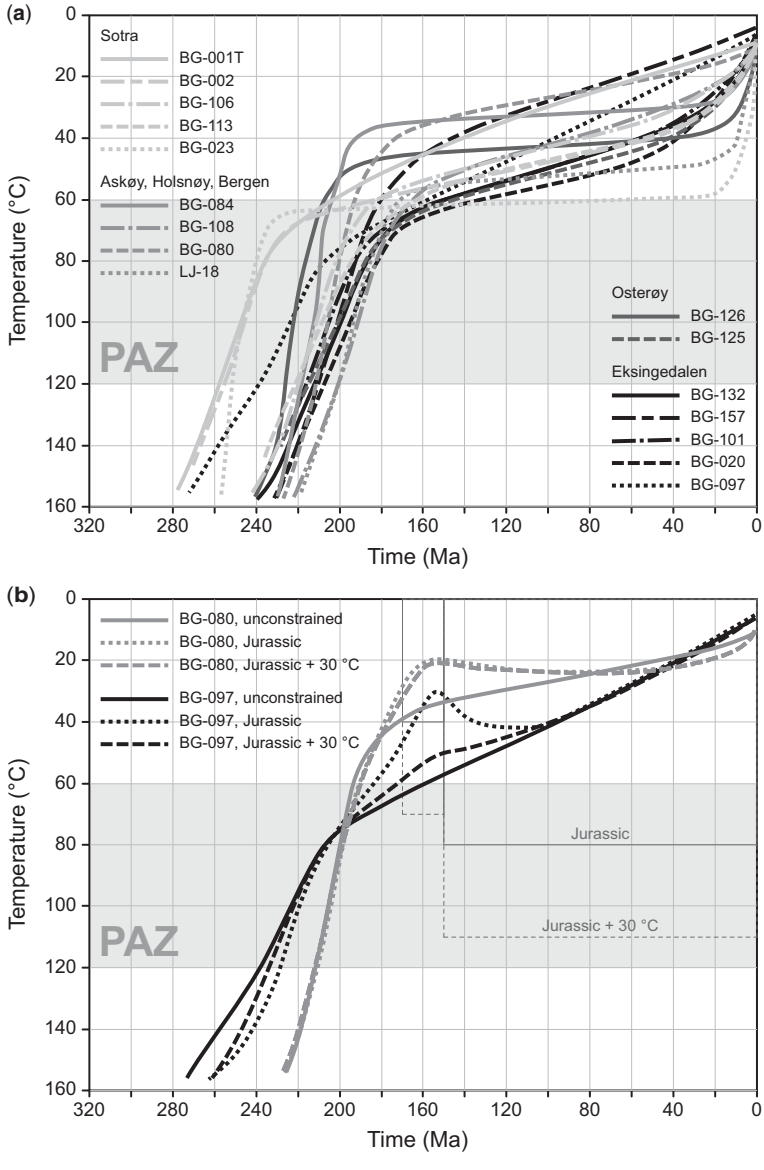

Fig. 6. Time–temperature models based on fission track ages and track lengths distributions. (U–Th)/He data are not included. Only the weighted mean paths are shown. (**a**) Only start and end constraints were used. Coastal samples in light grey, inland samples in black. Most samples show a change from fast to slow cooling in the early Jurassic. Inland samples cool through the partial annealing zone (PAZ) later and remain at higher temperatures in the Jurassic than coastal samples. (**b**) Comparison of coastal and inland samples (represented by BG-080 and BG-097, respectively). Boxes are modelling constraints. Both samples can be forced to the surface in the Jurassic (dotted paths). However, if given more freedom (extended boxes, Jurassic + 30 °C), coastal samples still cool to near-surface temperatures in the Jurassic (dashed grey path), while inland samples remain at depth and return to monotonous cooling histories (dashed black path) similar to the unconstrained models (solid black path).

through the apatite He partial retention zone in late Jurassic to Cretaceous times. On the other hand, the ages from the five samples that yielded significantly older modelled than measured ages need to be regarded with caution. The effect of radiation damage accumulation cannot account for the too old (U–Th)/He ages in these samples. As discussed above, we consider non-homogenous

eU-distributions the most likely cause, but the effect of eU-zonation on individual ages cannot be controlled.

Interpretation

Fission track and (U–Th)/He ages date the cooling of samples through the partial annealing/retention zone of respective thermochronological system, that is, *c.* 210–140 °C for the zircon (U–Th)/He system, *c.* 120–60 °C for apatite fission track system and *c.* 70–40 °C for the apatite (U–Th)/He system. The fission track ages suggest that some crustal blocks west of Bergen reached shallow crustal depths already in the Triassic. However, the majority of samples indicates cooling through the partial annealing zone of the fission track system in the early to middle Jurassic (Fig. 2), suggesting that the entire area was subjected to exhumation at that time. The fission track ages are thought to reflect relatively rapid uplift following Permo-Triassic North Sea rifting, whereas the (U–Th)/He ages mostly reflect much slower late Jurassic–Cretaceous cooling. This is reflected in the much greater dispersion of the apatite (U–Th)/He ages compared with the fission track ages.

While both fission track and apatite (U–Th)/He age become slightly younger towards the inland, the zircon (U–Th)/He ages increase away from the coast. Consequently, the age difference between apatite ages (fission track and (U–Th)/He) and zircon (U–Th)/He ages is relatively small at the coast and increases towards the inland. The tight cluster of Triassic to Jurassic ages from all three systems in the coastal samples again highlights the effect of rapid exhumation following Permo-Triassic North Sea rifting. In the inland, the zircon (U–Th)/He ages are older because the area experienced less pronounced erosion during Mesozoic rifting.

Typically, a positive correlation between fission track ages and elevation is expected within a structurally undisturbed crustal block. The absence of any correlation in our data is an obvious indication that the distribution of fission track ages is strongly controlled by tectonic structures that segment the area. This is confirmed by the presence of large age differences over short distances that are locally correlated with known faults. Similar conclusions can be drawn from the apatite (U–Th)/He ages. The offset across faults seems to be even more pronounced than in the fission track ages. However, this interpretation has to be taken with a grain of salt, since the (U–Th)/He ages are subject to the effects of grain size, eU-concentration and inhomogeneities in the eU-distribution and cannot always be compared directly. Nevertheless, both fission track and apatite (U–Th)/He ages are offset across the Hjeltefjorden Fault Zone (Fig. 2), indicating that this fault zone must have been active during Mesozoic times when differential uplift of the blocks on either side of the fault occurred. The NNW–SSE-striking Hjeltefjorden Fault Zone is part of an extensive array of similarly striking faults in the Sotra area that formed during east–west extension prior to or during Permian dyke intrusion at *c.* 260 Ma (Larsen *et al.* 2003). The Jurassic sediments preserved in a branch of the Hjeltefjorden Fault Zone cutting the Bjorøy Tunnel show that movement along the Hjeltefjorden Fault Zone occurred periodically at least until late Jurassic times (Fossen *et al.* 1997). This interpretation is now supported by thermochronological data presented here and is further in agreement with new K/Ar illite data of fault gouges from southwestern Norway, which indicate periods of fault activity in late Triassic to early Jurassic and Cretaceous to early Palaeogene times (Ksienzyk 2012; Ksienzyk *et al.* 2012). Along the Hjeltefjorden Fault Zone and parallel faults, older ages are exposed to the east of the faults, indicating down-to-the-east movement. This is in accordance with geological field evidence, which is also indicating down-to-the-east displacement (Fossen 1998). The Hjeltefjorden Fault Zone is thus a long-standing structural discontinuity that was repeatedly reactivated with a down-to-the-east sense of movement from Permian to at least Cretaceous times. Additionally, significant offsets in the apatite (U–Th)/He ages were observed across Herdlefjorden and across an unnamed fault in Eksingedalen (most likely one running through Steinslandsvatnet further north, here referred to as the Steinslandsvatnet Fault). Along both of these faults, older ages are exposed to the west of the fault, indicating down-to-the-west movement.

Thermal history modelling

Fission track lengths were measured in 16 samples, including the 12 samples selected for (U–Th)/He analysis. Inverse time–temperature modelling, based only on the fission track length distributions, was performed for all these samples with only start and end constraints. The resulting models show generally similar cooling patterns, with higher cooling rates (2–3 °C Ma^{-1}) in the Permian to Triassic and much slower cooling rates (<1 °C Ma^{-1}) since the Jurassic (Fig. 6a). The slowing of cooling occurs for most samples in the early Jurassic and at temperatures between 60 and 70 °C. A comparison of temperatures during middle Jurassic times shows generally higher temperatures for inland samples, indicating that these experienced more post-Jurassic erosion than coastal samples. Accordingly, the inland samples also cooled

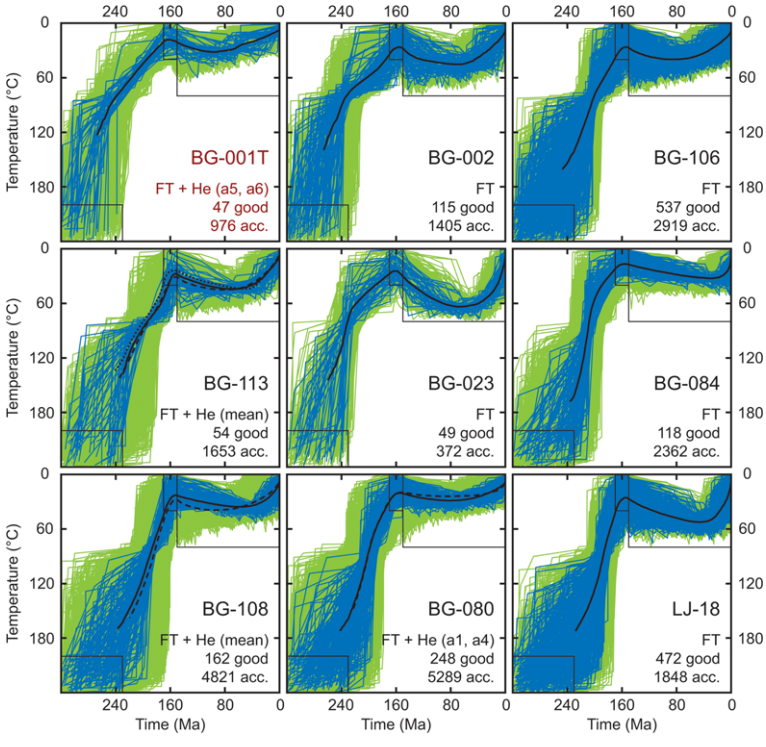

Fig. 7. Time–temperature models based on fission track and (U–Th)/He data. For each sample, the best possible model is shown. When (U–Th)/He data are included, this is specified under the sample name (FT, fission track; He, (U–Th)/He). In parentheses the (U–Th)/He data that were used for the modelling are specified: mean, sample mean values; a#, aliquot numbers referring to Table 2. For each model, 100 000 random paths were generated. The number of good (blue) and acceptable (green) paths is given. Solid black paths denote the weighted mean paths for the models shown; dashed black paths, weighted mean paths from alternative models based only on the fission track data from the respective sample; dotted black paths, weighted mean paths from other alternative models. The following alternative models are shown: BG-113 model is based on FT + He (a1, a6) and yielded no good paths but 382 acceptable paths; BG-125 model is based on FT + He (mean) but with a homogeneous U-distribution and yielded no good paths and only 20 acceptable paths; BG-157 model is based on FT + He (a2, a5) and yielded no good paths but 129 acceptable paths. Geological constraints imposed on the models are represented by boxes outlined in black. The three samples with the most robust fission track-(U–Th)/He data pairs are highlighted with red sample numbers.

through the partial annealing zone later than the coastal samples. Many of the samples show a second episode of faster cooling in the Cenozoic (1–2 °C Ma^{-1}), although the onset of this is generally poorly constrained.

A second suite of models includes constraints forcing the samples to the surface in the Jurassic and allowing for subsequent reburial (Figs 6b & 7). Coastal samples again show relatively rapid cooling until the Jurassic, which is now followed by mild reburial and renewed cooling to surface temperatures. Most samples show reheating during sedimentary burial to temperatures around 30–50 °C, which is in accordance with the vitrinite reflectance data from the Bjorøy Formation (Fossen *et al.* 1997). The time when the samples reach their maximum temperature varies from mid-Cretaceous to late Palaeogene, but falls into the late Cretaceous for most samples, thus coinciding with the period of the highest sea-levels. Generally, the westernmost samples from Sotra show the highest post-Jurassic temperatures (on average 44 °C) and thus deepest burial. Maximum burial temperatures decrease towards the inland to 32–39 °C on Askøy and <30 °C for sample BG-080 from Holsnøy. It can therefore be speculated that the sediment cover significantly thinned away from the coast and did not exceed a few hundred metres of thickness in the Holsnøy/Lindås area. For samples further east, the maximum temperatures increase again to around 50 °C. We consider it unlikely that the sediment thickness increased towards the

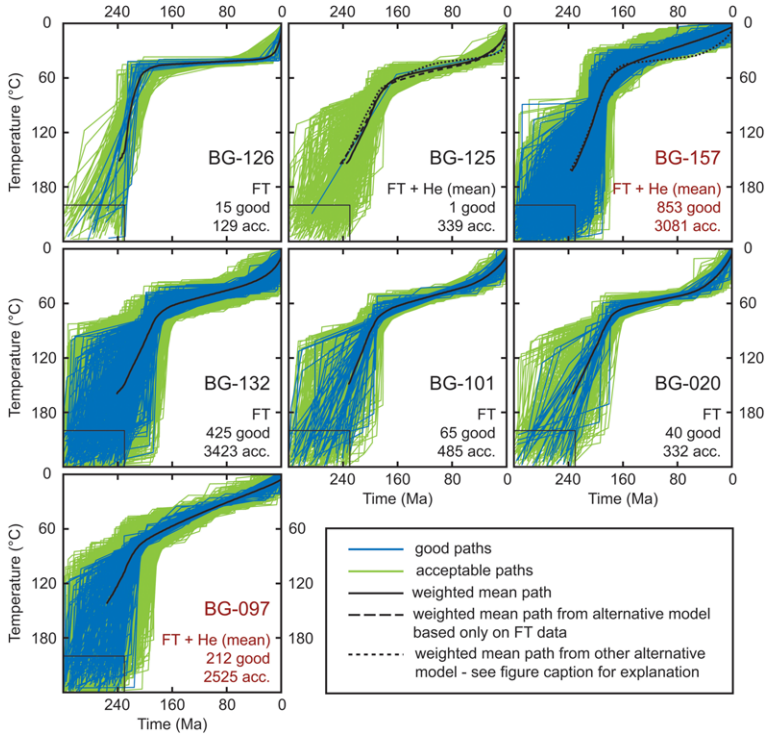

Fig. 7. *Continued.*

inland. While these models are numerically possible, we consider them to be geologically unreasonable. Hence models not forcing the samples to the surface in the Jurassic are preferred for samples east of sample BG-080. This interpretation is also supported by modelling runs using the Jurassic constraints but extending them to higher temperatures by 30 °C (Fig. 6b). These settings allow the samples to either reach the surface in the Jurassic or remain buried. While coastal samples tend to cool to the surface in the Jurassic, followed by reburial, inland samples return to the simpler, monotonous cooling histories of the unconstrained models when given the chance (Fig. 6b). The break between 'coastal' and 'inland' samples between samples BG-080 and BG-126 coincides approximately with a change in topography: east of sample BG-080, the topography becomes significantly rougher with peaks around and above 1000 m.

As discussed above, apatite (U–Th)/He data were modelled together with the fission track data for seven of the samples. For five of these samples with positive correlations between age and eU, two single apatites from the upper and lower end of the eU-spectrum were modelled together, in order to obtain the best constrained time–temperature solutions. This yielded numerous good and acceptable paths for samples BG-001T and BG-080 and these models are shown in Figure 7. For the other samples no good paths, and in some cases not even acceptable paths, were found. For those samples as well as the two samples showing no or negative correlations of age with eU, the mean sample (U–Th)/He age, grain size and U-, Th- and Sm-concentrations were used for the modelling. However, weighted mean paths from the models based on single-grain apatite data are shown for comparison if they yielded acceptable paths (BG-113 and BG-157, Fig. 7). For sample BG-125, a zoning profile was generated to compensate for the inhomogeneous U-distribution in the sample. A core with 30 ppm U and 14 ppm Th comprising 60% of the grain radius and surrounded by a rim with 4 ppm U and 1.4 ppm Th satisfies both the total U- and Th-compositions of the sample and the zoning geometries observed on the fission track mount (Fig. 5). For comparison, the weighted mean path for the same model but with a homogeneous U-distribution is shown in Figure 7.

While the addition of the (U–Th)/He data helps to constrain the models better, especially in the

low-temperature part, the general cooling histories remain the same. Figure 7 presents well the different cooling patterns for coastal and inland samples: coastal samples experienced large amounts of rapid uplift from Permian to early Jurassic times, followed by prolonged residence near the surface, including shallow reburial. The inland samples are characterized by initially slower uplift that persisted throughout the Mesozoic and Cenozoic. They did not reach the surface until Cenozoic times and experienced significantly more post-Jurassic exhumation than the coastal samples.

Summary

The fission track and (U–Th)/He ages presented here reflect predominantly the effect of Permian to Jurassic North Sea rifting. Changes in exhumation rates both geographically (coast v. inland) and temporally (e.g. pre- v. post-Jurassic for coastal samples) are well documented. Despite a relatively large scatter in ages and the considerable uncertainties associated with both methods, large age offsets over relatively short distances and at the same elevation are prominent in both fission track and (U–Th)/He data. Several of these offsets coincide with known faults. This highlights the importance of active fault tectonics in southwestern Norway throughout the entire Mesozoic.

Post-Caledonian evolution of SW Norway

The transformation of the Caledonian orogen into today's elevated passive margin is a long and complicated history of which many chapters remain poorly understood. Starting with a major continent–continent collisional orogen, it incorporates multiple periods of rifting that eventually failed in the North Sea but successfully led to the opening of the North Atlantic. Today's landscape is a product of this history, but how it formed is still highly controversial. In the following sections, we review available thermal constraints, summarize evidence of brittle deformation and try to place the thermochronological data presented here into the bigger context of southwestern Norway's tectonomorphological evolution.

Thermal constraints

The earliest records from thermochronological systems come from $^{40}Ar/^{39}Ar$ and K/Ar analyses of hornblende, muscovite and biotite. These minerals record cooling through *c.* 500 °C, *c.* 425 °C and *c.* 300 °C respectively (McDougall & Harrison 1999; Harrison *et al.* 2009). Hornblende ages in southwestern Norway range from *c.* 420 to 395 Ma (Chauvet & Dallmeyer 1992; Boundy *et al.* 1996; Fossen & Dunlap 1998; Eide *et al.* 1999; Young *et al.* 2011). The majority of muscovite and biotite ages range from *c.* 420 to 385 Ma (Bryhni *et al.* 1971; Chauvet & Dallmeyer 1992; Berry *et al.* 1995; Fossen & Dallmeyer 1998; Fossen & Dunlap 1998, 2006; Eide *et al.* 1999; Walsh *et al.* 2007; Young *et al.* 2011). While the older ages (>405 Ma) are attributed to Caledonian thrusting (Fossen & Dunlap 1998, 2006), the younger ages record post-Caledonian extension or cooling. The proximity of all three thermochronometers highlights the rapid cooling through 500–300 °C in the early to middle Devonian. This is further documented in cooling paths modelled from $^{40}Ar/^{39}Ar$ K-feldspar data (Dunlap & Fossen 1998), which indicate rapid cooling in the early to middle Devonian to temperatures just below 300 °C, followed by a period of stability or slow cooling in the middle Devonian and Carboniferous. The $^{40}Ar/^{39}Ar$ K-feldspar data show a second period of increased cooling rates (to below 200 °C) in Permian and Triassic times. Latest Carboniferous to Triassic cooling to temperatures below 200 °C is also documented by zircon fission track ages (320–230 Ma, closure temperature *c.* 220 °C; Andriessen & Bos 1986; Leighton 2007; R. Kumar, pers. comm. 2010) and the zircon (U–Th)/He ages presented here (310–215 Ma, closure temperature *c.* 170 °C). Additionally, Fossen (1998) suggested temperatures of *c.* 150 °C during Permian (270–250 Ma) and Triassic (230–210 Ma) dyke intrusion. Dunlap & Fossen (1998) give cooling rates of *c.* 2.4–4.4 °C Ma^{-1} for the Permo-Triassic cooling event. These rates are only slightly higher than the 2–3 °C Ma^{-1} estimated Permo-Triassic cooling rates from the fission track and (U–Th)/He data presented here.

The Jurassic and Cretaceous brought a change in cooling rates and coastal and inland areas followed significantly different cooling paths: inland areas continued to cool slowly but steadily (<1 °C Ma^{-1}) until cooling rates picked up again in the Cenozoic. Coastal samples, on the other hand, were at or near the surface in the Jurassic and experienced mild reheating to temperatures of *c.* 30–50 °C owing to sedimentary burial. This corresponds to *c.* 1–2 km of sediment cover and similar values were also obtained from vitrinite reflectance data from the Bjorøy Formation (Fossen *et al.* 1997). The landward extent of the sedimentary cover is uncertain, but if it extended further east than the Holsnøy/Lindås area, the thermochronological data presented here suggest that it was most likely thin. Most samples reached maximum burial depths in the late Cretaceous followed by erosion of the sedimentary cover in the Cenozoic.

Brittle deformation

Faults formed and were active as soon as the region had cooled enough to allow for the onset of brittle deformation. The earliest brittle fault was dated on Sotra at 396 Ma by U/Pb analysis of titanite grown in a fault-related fracture (Larsen *et al.* 2003). Faults stayed active or were periodically reactivated throughout the Permo-Carboniferous and Mesozoic. Permian and late Jurassic to early Cretaceous faulting have been dated palaeomagnetically in fault rocks belonging to the Lærdal–Gjende Fault System and the Nordfjord–Sogn Detachment Zone and by $^{40}Ar/^{39}Ar$ dating of breccias in the latter (Torsvik *et al.* 1992; Eide *et al.* 1997; Andersen *et al.* 1999). K/Ar dating of illite from fault gouges in the present study area indicates periods of fault activity in the early Carboniferous, Permian, late Triassic to early Jurassic and Cretaceous to early Palaeogene (Ksienzyk 2012; Ksienzyk *et al.* 2012). The preservation of Jurassic sediments in a fault zone in the Bjorøy tunnel confirms fault activity in or after the late Jurassic (Fossen *et al.* 1997). The fission track and (U–Th)/He ages presented here and in previously published studies (Redfield *et al.* 2004, 2005; Leighton 2007) also indicate fault movements throughout the entire Mesozoic and most likely well into the Cenozoic.

The tectonomorphological evolution of a 'not so passive' margin

The geomorphological evolution, particularly the topographic relief, is probably the most elusive component in the post-Caledonian history of southwestern Norway. A few relatively well-studied key events stand out in the development of the Norwegian continental margin: the Silurian to earliest Devonian Caledonian orogeny (e.g. Gee *et al.* 2008), Permo-Triassic and Jurassic rifting in the North Sea (e.g. Færseth 1996) and finally continental break-up and the opening of the North Atlantic in the early Palaeogene (e.g. Doré *et al.* 1999). The vast time between these events, however, is still obscured by knowledge gaps and controversy over existing data. Together with published ages, the thermochronological data presented here can help to distinguish between existing models.

At the end of the Caledonian orogeny, southwestern Norway was part of an extensive mountain range of possibly up to 8 km height (Gee *et al.* 2008, 2011; Streule *et al.* 2010). Immediately following the continent–continent collision, this mountain range quickly disintegrated by rapid orogenic collapse in the early Devonian (e.g. Fossen 2010). Ultra-high-pressure eclogites in the Western Gneiss Region bear witness to enormous amounts of tectonic exhumation during these early stages of extension (Hacker *et al.* 2010). Crustal-scale extensional structures, such as the Nordfjord–Sogn Detachment Zone, controlled the exhumation of these deep crustal rocks in their footwall, while intermontane basins filled with mostly coarse clastic sediments formed in their hanging walls (Seranne & Seguret 1987). To what extent the Caledonian mountains were removed during these early stages of collapse is contentious. Cooling rates dropped during the Carboniferous (Dunlap & Fossen 1998), but faults were still active (Ksienzyk *et al.* 2012). In the absence of any major post-Caledonian crust-thickening events, and assuming the crust was thinned during Permo-Triassic rifting, we can speculate that the crust during the (pre-rift) Carboniferous period was thicker than it is today and might well have supported an elevated topography.

The onset of rifting in the North Sea and North Atlantic in the Permian marks a new stage in the evolution of the Norwegian continental margin. Magmatism and rifting in the Oslo Rift occurred in the uppermost Carboniferous and Permian (e.g. Neumann *et al.* 1992, 2004; Larsen *et al.* 2008). While not as well documented, it is reasonable to believe that rifting in the northern North Sea was also initiated in the Permian (Gabrielsen *et al.* 1990; Færseth 1996; Ksienzyk 2012). The Permo-Triassic rifting event in the North Sea was widespread and centred on the Horda Platform just offshore southwestern Norway (Færseth *et al.* 1995; Færseth 1996). Its effect on onshore areas was therefore considerable. Increased Permo-Triassic cooling rates obtained both from modelling of Ar/Ar K-feldspar data (Dunlap & Fossen 1998) and the fission track and (U–Th)/He data presented here and in previous studies (Rohrman *et al.* 1995; Redfield *et al.* 2004, 2005; Hendriks *et al.* 2007; Leighton 2007) document onshore rift flank uplift and erosion. Coastal areas of southwestern Norway were intruded by Permian dykes (Færseth *et al.* 1976; Løvlie & Mitchell 1982; Torsvik *et al.* 1997; Fossen & Dunlap 1999) and fault activity was widespread (Torsvik *et al.* 1992; Eide *et al.* 1997; Andersen *et al.* 1999; Larsen *et al.* 2003; Ksienzyk 2012; Ksienzyk *et al.* 2012). While the Permo-Triassic thinning of the crust in onshore southwestern Norway was much less than that of the offshore Horda Platform, some thinning must have occurred owing to both extensional deformation and increased erosion of the uplifted rift flanks. There is no doubt that during the Triassic, and probably also the Jurassic, the topographic relief in southwestern Norway was still relatively high. Thick deposits of Triassic and Jurassic clastic sediments off the coast of southwestern Norway were derived from the Norwegian mainland (e.g. Evans *et al.* 2003; and references therein) and some

relief in the source area is needed to provide that much clastic material. Paul *et al.* (2008, 2009) used K/Ar dating of detrital micas to show that Caledonian-aged detritus derived from southern Norway was transported far and wide across the European continent during late Triassic times and concluded that southern Norway must have experienced considerable amounts of uplift at this time. Sømme *et al.* (2013) used the volume of point-sourced depocentres along the Norwegian margin, to make predictions about the hinterland topography and suggested a maximum relief of 1.6 km for the late Jurassic. Thermal modelling shows that the rocks exposed in the coastal areas of southwestern Norway have resided close to the surface since the middle Jurassic. With onshore uplift and offshore deposition and subsidence, these coastal areas must have acted as a relatively stable hinge zone. The differential movement between offshore and onshore areas is at least partially compensated by down-to-the-west faulting, as suggested by the (U–Th)/He data.

The Cretaceous is often envisioned as a period of subdued topography with only several hundred metres maximum relief (Gabrielsen *et al.* 2010*a*; Sømme *et al.* 2013) or even as a time of complete peneplanation and possibly even sedimentary burial in southern Norway (e.g. Lidmar-Bergström *et al.* 2000). While thermochronological data do not provide direct information on topographic relief, the data presented here place some constraints on these models: (a) the thermal history solutions for the inland samples do not favour a sedimentary cover; and (b) the slow but steady Jurassic to Palaeogene cooling requires actual exhumation rather than the surface uplift that would be required to move a peneplain formed at sea-level to elevations >1000 m. Furthermore, post-Jurassic fault activity is well documented by the data presented here and in previously published studies (Eide *et al.* 1997; Fossen *et al.* 1997; Ksienzyk 2012). These observations seem to be inconsistent with complete peneplanation and tectonic quiescence during the Cretaceous.

Altogether, the post-Caledonian evolution of southwestern Norway is strongly linked to the development of the North Sea rift basin. Fast Permo-Triassic cooling, which is particularly pronounced in the coastal samples, as well as Permo-Triassic fault activity can be directly related to rift flank uplift and erosion. The late Jurassic rift event in the North Sea was focused farther west in the Viking Graben (Færseth *et al.* 1995; Færseth 1996) and affected southwestern Norway to a lesser degree. This is reflected in significantly slower cooling rates at this time. When rifting in the North Sea ceased at the dawn of the Cretaceous (e.g. Doré *et al.* 1999), uplift of inland areas continued only slowly. However, faults were still active during the Cretaceous and most likely well into the Cenozoic, controlling slow differential uplift of fault-bound crustal blocks. Tectonic activity thus far outlived active rifting, and the question arises what mechanism was driving these fault movements. Redfield & Osmundsen (2013) attributed them to isostatically driven vertical adjustments in response to severe crustal thinning during a post-extensional accommodation phase.

To return to the different models of landscape evolution, the slow but persistent uplift documented by the inland samples seems to favour the ICE hypothesis (Nielsen *et al.* 2009*b*). However, it has to be pointed out that these samples were collected in valleys (with the exception of sample BG-157) at least several hundred metres below any suggested peneplanation surface and are therefore not ideally suited to solving this problem. Johannessen (2012) revisited the much studied Eidfjord area with new apatite fission track and (U–Th)/He dating, including much steeper vertical profiles, and came to the conclusion that Hardangervidda is not an old erosion surface. Samples residing at the surface today were most likely not exhumed until the Cenozoic. Similar conclusions were reached by Steer *et al.* (2012), who predicted that high-elevation, low-relief surfaces like Hardangervidda experienced considerable erosion even throughout Pliocene and Quaternary times.

Most importantly though, any model that claims to offer a valid tectonomorphological history of southwestern Norway needs to include active fault tectonics. Both the ICE hypothesis (Nielsen *et al.* 2009*b*) and the various peneplanation-uplift models have so far failed to take this properly into account. The close links between onshore thermal histories, fault activity and offshore tectonics provide support for Osmundsen & Redfield's (2011) and Redfield & Osmundsen's (2013) crustal taper hypothesis, linking Norway's topography to rift- and post-rift tectonics. Active faulting certainly provides a mechanism to modify the landscape and increase the topographic relief. We suggest therefore that there is no need to decide between either a long-standing high mountain range or total peneplanation. The evolution of the landscape and topographic relief of southwestern Norway was probably much more dynamic and closely connected to fault tectonics. The topography was repeatedly rejuvenated during periods of fault activity and subsequent footwall uplift, only to be worn down again by erosional processes.

Conclusions

Apatite fission track and apatite and zircon (U–Th)/He data from southwestern Norway reveal both

regional and temporal changes in cooling rates. Rapid cooling in the Permian to early Jurassic (*c.* 2–3 °C Ma^{-1}) is most pronounced in coastal samples and is closely related to rift tectonics in the North Sea and subsequent rift flank uplift and erosion. Coastal samples resided close to the surface since the Jurassic and experienced mild sedimentary reburial and heating to temperatures of 30–50 °C during the Cretaceous to earliest Palaeogene. Inland samples, on the other hand, were less affected by Permo-Triassic rifting. They continued to cool slowly (<1 °C Ma^{-1}) throughout the Jurassic and Cretaceous and did not reach the surface until the Cenozoic.

The distribution of both fission track and (U–Th)/He ages is tectonically controlled, highlighting the importance of fault reactivation throughout the entire Mesozoic. Active fault tectonics, together with the continuous exhumation documented by thermochronological data from inland samples, suggests that the tectonomorphological evolution of southwestern Norway was more dynamic than predicted by previous models and is strongly linked to rift- and post-rift tectonics. Episodes of fault activity and subsequent footwall uplift, increasing topographic relief, were interspersed with periods dominated by erosion leading to a more subdued relief. The elevated topography observed in southwestern Norway today is a product of this complex history.

A. K. Ksienzyk's work was funded through a PhD scholarship from the University of Bergen, which is gratefully acknowledged. Further support from the University of Bergen's Earth System Modelling Project (funded by Statoil) is equally gratefully recognized. We thank T. F. Redfield and P. A. M. Andriessen for positive but constructively critical reviews. The volume editor, F. Corfu, is thanked for his patience and encouragement, and efficient handling of the manuscript.

References

Andersen, T. B. 2011. Lower crustal processes during collision and exhumation: feedback between the ancient Caledonian and the modern Himalayan orogens. *Abstracts and Proceedings of the Geological Society of Norway*, **1**, 3.

Andersen, T. B., Torsvik, T. H., Eide, E. A., Osmundsen, P. T. & Faleide, J. I. 1999. Permian and Mesozoic extensional faulting within the Caledonides of central south Norway. *Journal of the Geological Society, London*, **156**, 1073–1080.

Andriessen, P. A. M. & Bos, A. 1986. Post-Caledonian thermal evolution and crustal uplift in the Eidfjord area, western Norway. *Norsk Geologisk Tidsskrift*, **66**, 243–250.

Bernet, M. 2009. A field-based estimate of the zircon fission-track closure temperature. *Chemical Geology*, **259**, 181–189.

Berry, H. N., Lux, D. R., Andresen, A. & Andersen, T. B. 1995. Progressive exhumation during orogenic collapse as indicated by $^{40}Ar/^{39}Ar$ cooling ages from different structural levels, southwest Norway. *Geonytt*, **22**, 20–21.

Boundy, T. M., Essene, E. J., Hall, C. M., Austrheim, H. & Halliday, A. N. 1996. Rapid exhumation of lower crust during continent–continent collision and late extension: evidence from $^{40}Ar/^{39}Ar$ incremental heating of hornblendes and muscovites, Caledonian orogen, western Norway. *Geological Society of America Bulletin*, **108**, 1425–1437.

Bryhni, I., Fitch, F. J. & Miller, J. A. 1971. $^{40}Ar/^{39}Ar$ dates from recycled Precambrian rocks in the Gneiss Region of the Norwegian Caledonides. *Norsk Geologisk Tidsskrift*, **51**, 391–406.

Chalmers, J. A., Green, P., Japsen, P. & Rasmussen, E. S. 2010. The Scandinavian mountains have not persisted since the Caledonian orogeny. A comment on Nielsen et al. (2009a). *Journal of Geodynamics*, **50**, 94–101.

Chauvet, A. & Dallmeyer, R. D. 1992. $^{40}Ar/^{39}Ar$ mineral dates related to Devonian extension in the southwestern Scandinavian Caledonides. *Tectonophysics*, **210**, 155–177.

Donelick, R. A., O'Sullivan, P. B. & Ketcham, R. A. 2005. Apatite fission-track analysis. *Reviews in Mineralogy and Geochemistry*, **58**, 49–94.

Doré, A. G., Lundin, E. R., Jensen, L. N., Birkeland, Ø., Eliassen, P. E. & Fichler, C. 1999. Principal tectonic events in the evolution of the northwest European Atlantic margin. *In*: Fleet, A. J. & Boldy, S. A. R. (eds) *Petroleum Geology of Northwest Europe: Proceedings of the 5th Conference*. Geological Society, London, 41–61.

Dumitru, T. A. 1993. A new computer-automated microscope stage system for fission-track analysis. *Nuclear Tracks and Radiation Measurements*, **21**, 557–580.

Dunkl, I. 2002. TRACKKEY: a Windows program for calculating and graphical presentation of fission track data. *Computers & Geosciences*, **28**, 3–12.

Dunlap, W. J. & Fossen, H. 1998. Early Paleozoic orogenic collapse, tectonic stability, and late Paleozoic continental rifting revealed though thermochronology of K-feldspars southern Norway. *Tectonics*, **17**, 604–620.

Eide, E. A., Torsvik, T. H. & Andersen, T. B. 1997. Absolute dating of brittle fault movements: late Permian and late Jurassic extensional fault breccias in western Norway. *Terra Nova*, **9**, 135–139.

Eide, E. A., Torsvik, T. H., Andersen, T. B. & Arnaud, N. O. 1999. Early Carboniferous unroofing in western Norway: a tale of alkali feldspar thermochronology. *The Journal of Geology*, **107**, 353–374.

Evans, D., Graham, C., Armour, A. & Bathurst, P. 2003. *The Millennium Atlas: Petroleum Geology of the Central and Northern North Sea, London*. Geological Society, London.

Færseth, R. B. 1996. Interaction of Permo-Triassic and Jurassic extensional fault-blocks during the development of the northern North Sea. *Journal of the Geological Society, London*, **153**, 931–944.

Færseth, R. B., Macintyre, R. M. & Naterstad, J. 1976. Mesozoic alkaline dykes in the Sunnhordland

region, western Norway: ages, geochemistry and regional significance. *Lithos*, **9**, 331–345.

FÆRSETH, R. B., GABRIELSEN, R. H. & HURICH, C. A. 1995. Influence of basement in structuring of the North Sea basin, offshore southwest Norway. *Norsk Geologisk Tidsskrift*, **75**, 105–119.

FARLEY, K. A., WOLF, R. A. & SILVER, L. T. 1996. The effects of long alpha-stopping distances on (U–Th)/He ages. *Geochimica et Cosmochimica Acta*, **60**, 4223–4229.

FARLEY, K. A., SHUSTER, D. L. & KETCHAM, R. A. 2011. U and Th zonation in apatite observed by laser ablation ICPMS, and implications for the (U–Th)/He system. *Geochimica et Cosmochimica Acta*, **75**, 4515–4530.

FLOWERS, R. M. & KELLEY, S. A. 2011. Interpreting data dispersion and 'inverted' dates in apatite (U–Th)/He and fission-track datasets: an example from the US midcontinent. *Geochimica et Cosmochimica Acta*, **75**, 5169–5186.

FLOWERS, R. M., KETCHAM, R. A., SHUSTER, D. L. & FARLEY, K. A. 2009. Apatite (U–Th)/He thermochronometry using a radiation damage accumulation and annealing model. *Geochimica et Cosmochimica Acta*, **73**, 2347–2365.

FOSSEN, H. 1998. Advances in understanding the post-Caledonian structural evolution of the Bergen area, West Norway. *Norsk Geologisk Tidsskrift*, **78**, 33–46.

FOSSEN, H. 2000. Extensional tectonics in the Caledonides: synorogenic or postorogenic. *Tectonics*, **19**, 213–224.

FOSSEN, H. 2010. Extensional tectonics in the North Atlantic Caledonides: a regional view. *In*: LAW, R. D., BUTLER, R. W. H., HOLDSWORTH, R. E., KRABBENDAM, M. & STRACHAN, R. A. (eds) *Continental Tectonics and Mountain Building: The Legacy of Peach and Horne*. Geological Society, London, Special Publications, **335**, 767–793.

FOSSEN, H. & DALLMEYER, R. D. 1998. $^{40}Ar/^{39}Ar$ muscovite dates from the nappe region of southwestern Norway: dating extensional deformation in the Scandinavian Caledonides. *Tectonophysics*, **285**, 119–133.

FOSSEN, H. & DUNLAP, W. J. 1998. Timing and kinematics of Caledonian thrusting and extensional collapse, southern Norway: evidence from $^{40}Ar/^{39}Ar$ thermochronology. *Journal of Structural Geology*, **20**, 765–781.

FOSSEN, H. & DUNLAP, W. J. 1999. On the age and tectonic significance of Permo-Triassic dikes in the Bergen-Sunnhordland region, southwestern Norway. *Norsk Geologisk Tidsskrift*, **79**, 169–178.

FOSSEN, H. & DUNLAP, W. J. 2006. Age constraints on the late Caledonian (Scandian) deformation in the Major Bergen Arc, SW Norway. *Norwegian Journal of Geology*, **86**, 59–70.

FOSSEN, H., MANGERUD, G., HESTHAMMER, J., BUGGE, T. & GABRIELSEN, R. H. 1997. The Bjorøy Formation: a newly discovered occurrence of Jurassic sediments in the Bergen Arc System. *Norsk Geologisk Tidsskrift*, **77**, 269–287.

GABRIELSEN, R. H., FÆRSETH, R. B., STEEL, R. J., IDIL, S. & KLØVJAN, O. S. 1990. Architectural styles of basin fill in the northern Viking Graben. *In*: BLUNDELL, D. J. & GIBBS, A. D. (eds) *Tectonic Evolution of the North Sea Rifts*. Clarendon Press, Oxford, 158–179.

GABRIELSEN, R. H., FALEIDE, J. I., PASCAL, C., BRAATHEN, A., NYSTUEN, J. P., ETZELMULLER, B. & O'DONNELL, S. 2010*a*. Latest Caledonian to present tectonomorphological development of southern Norway. *Marine and Petroleum Geology*, **27**, 709–723.

GABRIELSEN, R. H., FALEIDE, J. I., PASCAL, C., BRAATHEN, A., NYSTUEN, J. P., ETZELMULLER, B. & O'DONNELL, S. 2010*b*. Reply to discussion of Gabrielsen *et al.* (2010) by Nielsen et al. (this volume): Latest Caledonian to present tectonomorphological development of southern Norway. *Marine and Petroleum Geology*, **27**, 1290–1295.

GALBRAITH, R. E. ('Tracker') 1997. A negative association. *OnTrack*, **7**, 3–7.

GALBRAITH, R. F. 2005. *Statistics for Fission Track Analysis*. Chapman & Hall/CRC, Boca Raton.

GAUTHERON, C., TASSAN-GOT, L., KETCHAM, R. A. & DOBSON, K. J. 2012. Accounting for long alpha-particle stopping distances in (U–Th–Sm)/He geochronology: 3D modeling of diffusion, zoning, implantation, and abrasion. *Geochimica et Cosmochimica Acta*, **96**, 44–56.

GEE, D. G., FOSSEN, H., HENRIKSEN, N. & HIGGINS, A. K. 2008. From the early Paleozoic platforms of Baltica and Laurentia to the Caledonide Orogen of Scandinavia and Greenland. *Episodes*, **31**, 44–51.

GEE, D. G., JUHLIN, C., LADENBERGER, A. & CLAESSON, S. 2011. The North Atlantic Caledonides – a Himalaya–Tibet analogue. *Geological Society of America Abstracts with Programs*, **43**, 45.

GLEADOW, A. J. W. 1981. Fission-track dating methods: what are the real alternatives? *Nuclear Tracks*, **5**, 3–14.

GREEN, P. F. & DUDDY, I. R. 2006. Interpretation of apatite (U–Th)/He ages and fission track ages from cratons. *Earth and Planetary Science Letters*, **244**, 541–547.

GREEN, P. F., CROWHURST, P. V., DUDDY, I. R., JAPSEN, P. & HOLFORD, S. P. 2006. Conflicting (U–Th)/He and fission track ages in apatite: enhanced He retention, not anomalous annealing behaviour. *Earth and Planetary Science Letters*, **250**, 407–427.

HACKER, B. R., ANDERSEN, T. B., JOHNSTON, S., KYLANDER-CLARK, A. R. C., PETERMAN, E. M., WALSH, E. O. & YOUNG, D. 2010. High-temperature deformation during continental-margin subduction & exhumation: the ultrahigh-pressure Western Gneiss Region of Norway. *Tectonophysics*, **480**, 149–171.

HANSEN, K. & REINERS, P. W. 2006. Low temperature thermochronology of the southern East Greenland continental margin: evidence from apatite (U–Th)/He and fission track analysis and implications for intermethod calibration. *Lithos*, **92**, 117–136.

HARRISON, T. M., CÉLÉRIER, J., AIKMAN, A. B., HERMANN, J. & HEIZLER, M. T. 2009. Diffusion of ^{40}Ar in muscovite. *Geochimica et Cosmochimica Acta*, **73**, 1039–1051.

HENDRIKS, B. W. H. 2003. *Cooling and denudation of the Norwegian and Barents Sea margins, northern Scandinavia. Constrained by apatite fission track and (U–Th)/He thermochronology*. PhD thesis, Vrije Universiteit, Amsterdam.

HENDRIKS, B. W. H. & REDFIELD, T. F. 2005. Apatite fission track and (U–Th)/He data from Fennoscandia: an example of underestimation of fission track annealing in apatite. *Earth and Planetary Science Letters*, **236**, 443–458.

HENDRIKS, B. H. W. & REDFIELD, T. F. 2006. Reply to: comment on 'Apatite Fission Track and (U–Th)/He data from Fennoscandia: an example of underestimation of fission track annealing in apatite' by B. W. H. Hendriks and T. F. Redfield. *Earth and Planetary Science Letters*, **248**, 569–577.

HENDRIKS, B., ANDRIESSEN, P. *ET AL.* . 2007. A fission track data compilation for Fennoscandia. *Norwegian Journal of Geology*, **87**, 143–155.

HENDRIKS, B. W. H., OSMUNDSEN, P. T. & REDFIELD, T. F. 2010. Normal faulting and block tilting in Lofoten and Vesterålen constrained by apatite fission track data. *Tectonophysics*, **485**, 154–163.

HOURIGAN, J. K., REINERS, P. W. & BRANDON, M. T. 2005. U/Th zonation dependent alpha ejection in (U–Th)/He chronometry. *Geochimica et Cosmochimica Acta*, **96**, 3349–3365.

HURFORD, A. J. & GREEN, P. F. 1983. The zeta age calibration of fission-track dating. *Chemical Geology*, **41**, 285–317.

JOHANNESSEN, K. C. 2012. *Low-temperature thermochronological and structural study of the inner Hardangerfjord area, southern Norway*. MSc thesis, University of Bergen.

KETCHAM, R. A. 2005. Forward and inverse modelling of low-temperature thermochronometry data. *Reviews in Mineralogy and Geochemistry*, **58**, 275–314.

KETCHAM, R. A., CARTER, A., DONELICK, R. A., BARBARAND, J. & HURFORD, A. J. 2007*a*. Improved measurement of fission-track annealing in apatite using c-axis projection. *American Mineralogist*, **92**, 789–798.

KETCHAM, R. A., CARTER, A., DONELICK, R. A., BARBARAND, J. & HURFORD, A. J. 2007*b*. Improved modeling of fission-track annealing in apatite. *American Mineralogist*, **92**, 799–810.

KOHN, B. P., LORENCAK, M., GLEADOW, A. J. W., KOHLMANN, F., RAZA, A., OSADETZ, K. G. & SORJONEN-WARD, P. 2009. A reappraisal of low-temperature thermochronology of the eastern Fennoscandian Shield and radiation-enhanced fission-track annealing. *In*: LISKER, F., VENTURA, B. & GLASMACHER, U. A. (eds) *Thermochronological Methods: From Palaeotemperature Constraints to Landscape Evolution Models*. Geological Society, London, Special Publications, **324**, 193–216.

KSIENZYK, A. K. 2012. *From mountains to basins: geochronological case studies from southwestern Norway, Western Australia and East Antarctica.* PhD thesis, University of Bergen.

KSIENZYK, A. K., KOHLMANN, F., DUNKL, I., WEMMER, K., JACOBS, J. & FOSSEN, H. 2012. Late Caledonian orogenic collapse and Permian-Mesozoic rifting: dating onshore faults in SW Norway with low-temperature thermochronological methods. *Abstracts and Proceedings of the Geological Society of Norway*, **2**, 37.

LARSEN, B. T., OLAUSSEN, S., SUNDVOLL, B. & HEEREMANS, M. 2008. The Permo-Carboniferous Oslo Rift through six stages and 65 million years. *Episodes*, **31**, 52–58.

LARSEN, Ø., FOSSEN, H., LANGELAND, K. & PEDERSEN, R.-B. 2003. Kinematics and timing of polyphase post-Caledonian deformation in the Bergen area, SW Norway. *Norwegian Journal of Geology*, **83**, 149–165.

LARSON, S. Å., CEDERBOM, C. E., TULLBORG, E.-L. & STIBERG, J.-P. 2006. Comment on 'Apatite fission track and (U–Th)/He data from Fennoscandia: an example of underestimation of fission track annealing in apatite' by Hendriks and Redfield [Earth Planet. Sci. Lett. 236 (443–458)]. *Earth and Planetary Science Letters*, **248**, 561–568.

LEIGHTON, C. A. 2007. *The thermotectonic development of southern Norway: constraints from low-temperature thermochronology*. PhD thesis, Imperial College London.

LIDMAR-BERGSTRÖM, K. & BONOW, J. M. 2009. Hypotheses and observations on the origin of the landscape of southern Norway – a comment regarding the isostasy–climate–erosion hypothesis by Nielsen et al. 2008. *Journal of Geodynamics*, **48**, 95–100.

LIDMAR-BERGSTRÖM, K., OLLIER, C. D. & SULEBAK, J. R. 2000. Landforms and uplift history of southern Norway. *Global and Planetary Change*, **24**, 211–231.

LØVLIE, R. & MITCHELL, J. G. 1982. Complete remagnetization of some Permian dykes from western Norway induced during burial/uplift. *Physics of the Earth and Planetary Interiors*, **30**, 415–421.

MCDOUGALL, I. & HARRISON, T. M. 1999. *Geochronology and Thermochronology by the $^{40}Ar/^{39}Ar$ Method.* Oxford University Press, New York.

MEESTERS, A. G. C. A. & DUNAI, T. J. 2002. Solving the production–diffusion equation for finite diffusion domains of various shapes. Part II. Application to cases with α-ejection and nonhomogeneous distribution of the source. *Chemical Geology*, **186**, 347–363.

NEUMANN, E.-R., OLSEN, K. H., BALDRIDGE, W. S. & SUNDVOLL, B. 1992. The Oslo Rift: a review. *Tectonophysics*, **208**, 1–18.

NEUMANN, E.-R., WILSON, M., HEEREMANS, M., SPENCER, E. A., OBST, K., TIMMERMAN, M. J. & KIRSTEIN, L. 2004. Carboniferous-Permian rifting and magmatism in southern Scandinavia, the North Sea and northern Germany: a review. *In*: WILSON, M., NEUMANN, E.-R., DAVIES, G. R., TIMMERMAN, M. J., HEEREMANS, M. & LARSEN, B. T. (eds) *Permo-Carboniferous Rifting and Magmatism in Europe*. Geological Society, London, Special Publications, **223**, 11–40.

NIELSEN, S. B., GALLAGHER, K., EGHOLM, D. L., CLAUSEN, O. R. & SUMMERFIELD, M. 2009*a*. Reply to comment regarding the ICE-hypothesis. *Journal of Geodynamics*, **48**, 101–106.

NIELSEN, S. B., GALLAGHER, K. *ET AL.* . 2009*b*. The evolution of western Scandinavian topography: a review of Neogene uplift versus the ICE (isostasy–climate–erosion) hypothesis. *Journal of Geodynamics*, **47**, 72–95.

NIELSEN, S. B., CLAUSEN, O. R. *ET AL.* . 2010*a*. The ICE hypothesis stands: how the dogma of late Cenozoic tectonic uplift can no longer be sustained in the light of data and physical laws. *Journal of Geodynamics*, **50**, 102–111.

NIELSEN, S. B., CLAUSEN, O. R. *ET AL.* . 2010*b*. Discussion of Gabrielsen et al. (2010): Latest Caledonian to present tectonomorphological development of southern Norway. *Marine and Petroleum Geology*, **27**, 1285–1289.

OSMUNDSEN, P. T. & REDFIELD, T. F. 2011. Crustal taper and topography at passive continental margins. *Terra Nova*, **23**, 349–361.

PAUL, J., WEMMER, K. & AHRENDT, H. 2008. Provenance of siliciclastic sediments (Permian to Jurassic) in the Central European Basin. *Zeitung der Deutschen Gesellschaft für Geowissenschaften*, **159**, 641–650.

PAUL, J., WEMMER, K. & WETZEL, F. 2009. Keuper (Late Triassic) sediments in Germany – indicators of rapid uplift of Caledonian rocks in southern Norway. *Norwegian Journal of Geology*, **89**, 197–206.

PRIEM, H. N. A., BOELRIJK, N. A. I. M., HEBEDA, E. H., VERDURMEN, E. A. T. & VERSCHURE, R. H. 1976. Isotope geochronology of the Eidfjord Granite, Hardangervidda, West Norway. *Norges geologiske undersøkelse Bulletin*, **327**, 35–39.

REDFIELD, T. F. & OSMUNDSEN, P. T. 2013. The long-term topographic response of a continent adjacent to a hyperextended margin: a case study from Scandinavia. *GSA Bulletin*, **125**, 184–200.

REDFIELD, T. F., TORSVIK, T. H., ANDRIESSEN, P. A. M. & GABRIELSEN, R. H. 2004. Mesozoic and Cenozoic tectonics of the Møre Trøndelag Fault Complex, central Norway: constraints from new apatite fission track data. *Physics and Chemistry of the Earth*, **29**, 673–682.

REDFIELD, T. F., BRAATHEN, A., GABRIELSEN, R. H., OSMUNDSEN, P. T., TORSVIK, T. H. & ANDRIESSEN, P. A. M. 2005. Late Mesozoic to early Cenozoic components of vertical separation across the Møre–Trøndelag Fault Complex, Norway. *Tectonophysics*, **395**, 233–249.

RIIS, F. 1996. Quantification of Cenozoic vertical movements of Scandinavia by correlation of morphological surfaces with offshore data. *Global and Planetary Change*, **12**, 331–357.

ROHRMAN, M., VAN DER BEEK, P., ANDRIESSEN, P. & CLOETINGH, S. 1995. Meso-Cenozoic morphotectonic evolution of southern Norway: Neogene domal uplift inferred from apatite fission track thermochronology. *Tectonics*, **14**, 704–718.

SERANNE, M. & SEGURET, M. 1987. The Devonian basins of western Norway: tectonics and kinematics of an extending crust. *In*: COWARD, M. P., DEWEY, J. F. & HANCOCK, P. L. (eds) *Continental Extension Tectonics*. Geological Society, London, Special Publications, **28**, 537–548.

SHUSTER, D. L., FLOWERS, R. M. & FARLEY, K. A. 2006. The influence of natural radiation damage on helium diffusion kinetics in apatite. *Earth and Planetary Science Letters*, **249**, 148–161.

SÖDERLUND, P., JUEZ-LARRÉ, J., PAGE, L. M. & DUNAI, T. J. 2005. Extending the time range of apatite (U–Th)/He thermochronometry in slowly cooled terranes: Palaeozoic to Cenozoic exhumation history of southeast Sweden. *Earth and Planetary Science Letters*, **239**, 266–275.

SØMME, T. O., MARTINSEN, O. J. & LUNT, I. 2013. Linking offshore stratigraphy to onshore paleotopography: the Late Jurassic-Paleocene evolution of the south Norwegian margin. *Geological Society of America Bulletin*, **125**, 1164–1186.

STEER, P., HUISMANS, R. S., VALLA, P. G., GAC, S. & HERMAN, F. 2012. Bimodal Plio-Quaternary glacial erosion of fjords and low-relief surfaces in Scandinavia. *Nature Geoscience*, **5**, 635–639.

STREULE, M. J., STRACHAN, R. A., SEARLE, M. P. & LAW, R. D. 2010. Comparing Tibet-Himalayan and Caledonian crustal architecture, evolution and mountain building processes. *In*: LAW, R. D., BUTLER, R. W. H., HOLDSWORTH, R. E., KRABBENDAM, M. & STRACHAN, R. A. (eds) *Continental Tectonics and Mountain Building: The Legacy of Peach and Horne*. Geological Society, London, Special Publications, **335**, 207–232.

TORSVIK, T. H., STURT, B. A., SWENSSON, E., ANDERSEN, T. B. & DEWEY, J. F. 1992. Palaeomagnetic dating of fault rocks: evidence for Permian and Mesozoic movements and brittle deformation along the extensional Dalsfjord Fault, western Norway. *Geophysical Journal International*, **109**, 565–580.

TORSVIK, T. H., ANDERSEN, T. B., EIDE, E. A. & WALDERHAUG, H. J. 1997. The age and tectonic significance of dolerite dykes in western Norway. *Journal of the Geological Society, London*, **154**, 961–973.

WALSH, E. O., HACKER, B. R., GANS, P. B., GROVE, M. & GEHRELS, G. 2007. Protolith ages and exhumation histories of (ultra)high-pressure rocks across the Western Gneiss Region, Norway. *Geological Society of America Bulletin*, **119**, 289–301.

YOUNG, D. J., HACKER, B. R., ANDERSEN, T. B. & GANS, P. B. 2011. Structure and $^{40}Ar/^{39}Ar$ thermochronology of an ultrahigh-pressure transition in western Norway. *Journal of the Geological Society, London*, **168**, 887–898.